Measurement of Shock and Detonation Propagation Along Pentaerythritol Tetranitrate (PETN) Thin Films

by

Julio C. Peguero II

Submitted in Partial Fulfillment
of the Requirements for the Degree of
Master of Science in Mechanical Engineering
with a Specialization in Explosives Engineering

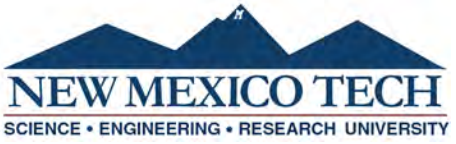

New Mexico Institute of Mining and Technology
Socorro, New Mexico
September, 2019

ABSTRACT

Physical vapor deposition is a method used to deposit films of pentaerythritol tetranitrate (PETN) with great control over microstructure. As a result of depositing high density PETN films, microcracking in the films frequently occurs. PETN detonation testing was conducted to determine the effect these microcracks have on detonation. To explore this, two films were separated by controlled gaps to simulate cracks in films. The detonation was initiated at the beginning of a film, and refractive imaging was used to determine whether the detonation successfully propagated across the gap. Films of various thicknesses were evaluated to determine the maximum gap width that would result in detonation propagation at a specified PETN film thicknesses.

The tests were also simulated with CTH. Computer generated schlieren (CGS) images were developed to provide a comparable evaluation to the experiments. With minimal effort in adjusting equation of state parameters, the CGS images were able to resemble the refractive images obtained from experimentation.

Keywords: PETN, Detonation, Explosive, Schlieren, Shadowgraph, CTH

ACKNOWLEDGMENTS

I would like to thank my advisor Michael Hargather for shaping me into the researcher I am today. I would like to thank Eric Forrest for his tremendous support and feedback. Without them I would not have been able to complete this thesis. I would also like to thank Otis Solomon for his DC reviewing efforts. I would like to thank Robert Knepper, Alex Tappan, Michael Marquez, Stephen Rupper, Jon Vasiliauskas and Caitlin O'Grady for their support with testing. I would also like to thank Cody Kirk for his great CTH advice. In addition I would like to thank Paul Shoemaker for starting the Campus Executive collaboration, that made this all possible.

I want to thank all the members of the Shock and Gas Dynamics Laboratory for making my time there enjoyable. Also for their great advice that helped me push my research further. I would like to thank my parents Julio and Christine for their endless support and encouragement.

This work was supported by the Laboratory Directed Research and Development program at Sandia National Laboratories, a multimission laboratory managed and operated by National Technology & Engineering Solutions of Sandia, LLC, a wholly owned subsidiary of Honeywell International, Inc., for the U.S. Department of Energy's National Nuclear Security Administration under contract DE-NA0003525.

This report describes objective technical results and analysis. Any subjective views or opinions that might be expressed in the paper do not necessarily represent the views of the U.S. Department of Energy or the United States Government. Unclassified, unlimited release SAND2019-2019-9412 T.

This thesis was typeset with LaTeX[1] by the author.

[1]The LaTeX document preparation system was developed by Leslie Lamport as a special version of Donald Knuth's TeX program for computer typesetting. TeX is a trademark of the American Mathematical Society. The LaTeX macro package for the New Mexico Institute of Mining and Technology thesis format was written by John W. Shipman.

CONTENTS

LIST OF TABLES

LIST OF FIGURES

Figure **Page**

This thesis is accepted on behalf of the faculty of the Institute by the following committee:

Michael J. Hargather

Academic and Research Advisor

Eric C. Forrest

Seokbin Lim

I release this document to the New Mexico Institute of Mining and Technology.

Julio C. Peguero II July 3, 2019

CHAPTER 1

INTRODUCTION

1.1 Motivation

Explosives are able to be deposited using physical vapor deposition (PVD). Depositing thin films of explosives allows for the study of explosive processes on an extremely small scale with films tens of microns thick. PVD allows for control over the microstructure of films. As a result of varying the surface energy of the substrate the films are deposited on, the density of the films can be controlled. When high density films are made, microcracking in the films can occur. Currently it is unknown what effect these microcracks have on the detonation propagation in thin films.

The research here will explore detonation propagation in thin films to understand the critical gap widths across which detonation can and cannot propagate. Experimental testing and computational modeling have been performed to determine the largest gap a film can have while maintaining detonation, and to understand the effect the gap causes on detonation.

1.2 Explosive Detonation

A detonation is a rapid combustion process driven by a shock front within an explosive [1, 2]. The Zeldovich, von Neumann, Döring (ZND) model is an ideal theory of detonation. This model makes the assumption that the flow is one dimensional, and the reaction zone length is negligible [1]. According to the ZND model a chemical reaction within an explosive is initiated by a shock wave propagating within the explosive. The explosive is heated and compressed as the shock wave passes through it, causing the chemical reaction. The energy produced by this chemical reaction drives the shock front, and thus the detonation. Gas products form as a result of the chemical reaction. The shock front, chemical reaction, and the rarefaction front travel together in equilibrium at a speed that is referred to as the detonation velocity [1].

1.3 Detonation Measurements

Typically, explosive detonation testing is performed on the macro-scale where kilograms of loose powder explosives are pressed into pellets of various shapes such as cylinders. The explosives are used for many purposes such as quantification of explosive output and detonation propagation characteristics. Properties such as density [3], temperature [4], pressure [5], particle velocity and detonation velocity are measured. Velocities are generally the easiest properties to measure [6]. The particle velocity can be used to determine the pressure at an interface with the use of Hugoniot properties [7].

Velocity interferometer system for any reflector (VISAR) [8] and Heterodyne velocimetry [9], also known as photon Doppler velocimetry, are commonly used for particle and free surface velocity measurements [7, 10]. These methods work by measuring the Doppler shift as the detonation interacts with a reflective surface. These methods are only able to measure the velocity off of a reflective surface and thus are not able to determine detonation velocity directly.

Detonation velocity can be measured by mechanical and ionization pin switches, which rely on closure of a circuit by contact of the pin to a displaced confinement wall and the ionization of the detonation front respectively [11].

Fiber optic probes with holes drilled at specified locations are able to determine position and time data from the ionization of the detonation front [12]. Continual measurements are possible with chirped fiber optic Bragg gratings (CFBG). The CFBG utilizes a 125 μm-diameter fiber optic placed in the center of the explosive. The detonation velocity is determined by the dependence of the reflectivity and the CFBG length [13, 14]. Electromagnetic waves are a non-intrusive method for determination of the detonation velocity. The Doppler shift is measured off the reflective surface of the ionization in the detonation front to determine detonation velocity [15].

There is a dependence of the detonation velocity on the diameter of the explosive, called the diameter effect. Campbell and Engelke tested for this by measuring the detonation velocity along cylinders of explosives using ionization switches at known increments [16]. The diameter is varied until detonation fails to propagate at a small enough diameter [16]. The diameter at which detonation fails to propagate is known as the critical diameter. There is another method to determine the critical diameter which only requires one test for each explosive. This test uses a cone shaped explosive, and the results of critical diameter are slightly lower than the previously mentioned test due to the detonation being in an overdriven state. The cone is initiated at the base and the critical diameter is determined to be the diameter at which the detonation fails. The determination of detonation failure in this test is by the use of a resistance probe placed in the center of the explosive as well as streak camera imaging [17].

In addition to the performance of explosives, failure is also of interest. One method commonly used is the gap test, of which there are several variations, including the Naval Surface Warfare Center (NSWC) small scale gap test, Los Alamos National Laboratory (LANL) small scale gap test, LANL large scale gap

test, Pantex Plant (PX) gap test, and the Stanford Research Institute (SRI) gap test [18, 19, 20]. Each test consists of a donor charge, acceptor charge, and an attenuator. The donor charge and the acceptor charge are separated by an attenuator of varying thickness. An explosive is found to be more sensitive with and increasing attenuator size that results in detonation of the acceptor charge. Detonation of the acceptor charge is determined by a dent made in a witness plate placed at the end of the acceptor charge [18].

At the sub-millimeter scale, subtle initiation effects can be isolated from the bulk detonation properties [21]. The removal of the bulk effects allows the study of initiation effects of films using multiple different configurations. However, pressing explosive powders is limited in the geometries and scales that can be produced. It is very difficult to press cylinders that are less than 2 mm in diameter [22]. It is also not possible to have precise control over the microstructure of the specimen with traditional pressing methods [23].

1.4 Physical Vapor deposition (PVD)

PVD is a process used to deposit thin films of elements, compounds or molecules, and has been shown to alleviate several issues with pressed explosives [23, 22]. PVD uses thermal vaporization to create a gas from the material of interest, which is then condensed onto a substrate. The process is performed under high vacuum to reduce the vapor pressure and to produce thin films with high purity [24].

Organic explosives such as pentaerythritol tetranitrate (PETN), hexanitroazobenzene (HNAB) [25] and hexanitrostilbene (HNS) [26] can be deposited by PVD. PETN is often studied due to its relatively low vapor pressures at easily obtainable vacuum levels, allowing for rapid deposition [23, 27]. PETN also has a small critical dimension that allows for deposition at a very small scale [23, 27]. The Department of Energy (DOE) classifies PETN as a secondary explosive which means it is relatively insensitive to initiation, which makes it relatively safe to work with [28].

It has been shown that the microstructure of PETN can be controlled through the variation of PVD deposition conditions [23]. The literature suggest that the microstructural properties such as density, pore size and distribution, ultimately effect the detonation velocity, initiation sensitivity, and the critical dimension. [23, 29, 30, 31, 18, 32].

PVD is limited in the geometries that can be produced; it is not possible to deposit a cylinder with PVD [22, 33]. The main configuration used in detonation testing is a slab configuration, although methods exists to create patterns [34, 35] or channels [34] within the films. PVD allows films to be developed that are close to their critical thickness [23, 22, 36]. This can lead to a better understanding of the failure mechanisms [33]. Also of interest is the study of initiation [21, 33], and shock response [33].

Even though the deposition of PETN is limited to slab configurations [33], the diameter effect still applies [36]. The diameter effect is the change in velocity due to energy losses from the side of the cylinder as the diameter or thickness, of the explosive changes [16, 1]. The critical dimension in cylinders, is the diameter at which the detonation fails to propagate as the diameter is reduced to the point where energy losses to the side of the column are larger than the energy produced in the explosive [1]. Although geometry differences exist between cylinders and slabs, the critical dimensions are similar. The critical thickness for a detonation of a slab has been shown to roughly be equal to half the critical diameter of a cylinder. The experimental data of Gibbs and Popolato [37] quantifying the failure thickness in explosives relates well to the data from Campbell and Engelke [16], and Dobratz [18] quantifying the failure diameter. There are some discrepancies in the ratio between the critical diameter and the critical thickness, due to slight differences in the composition of explosives used. Nevertheless, the ratio remains near one [38].

The alteration of the substrate surface energy has been demonstrated to change the density of PETN films. PETN films deposited onto substrates with higher surface energy have been shown to have higher density, which in turn increases the detonation velocity [39, 40].

One downside to producing high density PETN films with PVD is that microcracking can occur as shown in Fig. 1.1 [23, 39]. The cracking of the PETN films is due to compressive stresses in the films [23, 41]. The compressive stresses are likely due to the large difference in thermal expansion coefficient between the substrate and the PETN film [42].

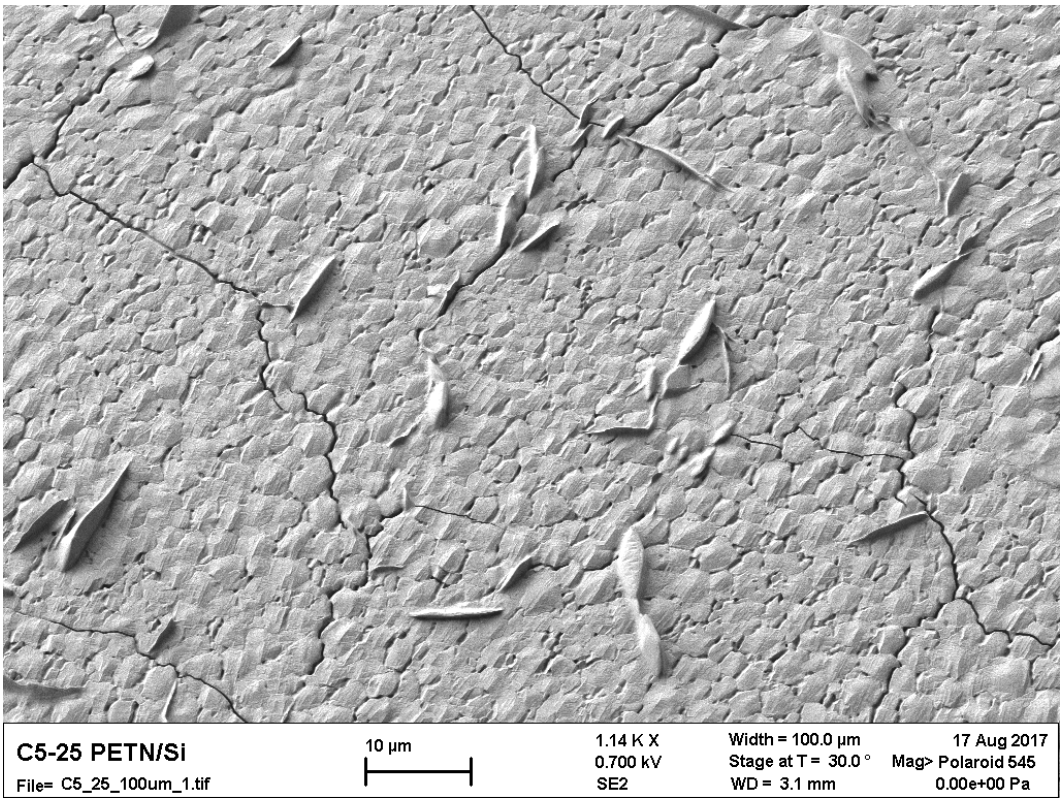

Figure 1.1: Scanning electron micrograph (SEM) of a dense PETN film displaying microcracking.

1.5 Explosive Diagnostics Using Refractive Imaging

Refractive imaging is useful for the study of explosive events because shock and detonation waves can be directly visualized. Refractive imaging is a class of imaging methods that allow the visualization of changes in the refractive index. The refractive index, n, is the ratio of the speed of light in a vacuum, c, to the speed of light in a transparent medium c_m:

$$n = \frac{c_m}{c} \tag{1.1}$$

Focused shadowgraph visualizes the second derivative of the refractive index field which provides a high sensitivity to shock waves, while being relatively insensitive to weak gas phenomena such as rarefactions. Schlieren imaging is a refractive imaging method that visualizes the first derivative of the refractive index field. This allows a high sensitivity to weak gas disturbances while still maintaining a high sensitivity to strong shock waves [43].

Focused shadowgraph imaging is achieved by the collimation of a point source of light. The light is then passed through a test section where the medium of interest is located. The light is then refocused to a point and the light enters a camera. A schematic of a focused shadowgraph system is shown in Fig. 1.2. This results in an image of the shadow of light refractions captured by the camera. Schlieren imaging can be achieved by the addition of a simple knife edge at the point where the light is focused after the second lens. The difference in the refractive index of the visualized media results in bending of light which is cut off by the knife edge resulting in a dark area in the image.

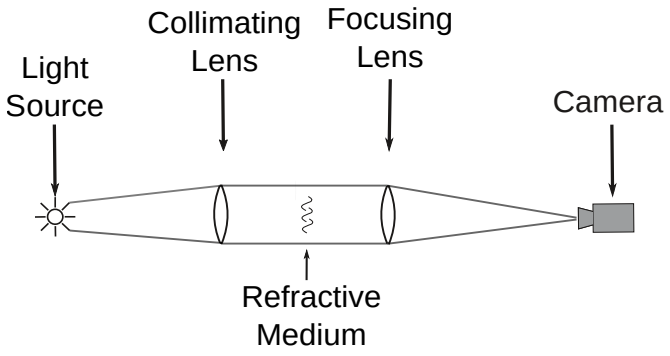

Figure 1.2: Schematic of a focused shadowgraph system.

Refractive imaging has been widely used in explosive research due to its simplicity and the ability to produce images of shock waves. There have been many instances for the use of refractive imaging to visualize shock waves in air [44, 45] and in solids [46, 47, 48, 49]. Specifically of interest, refractive imaging has been used on a relatively small scale to characterize detonators [47, 50, 48, 49]. Refractive imaging can also be applied with cameras in stereo to extract three-dimensional shock position [51]. It is even sensitive enough to image the shock waves produced by the deflagration of pyrotechnics [52].

1.6 Simulation of Explosive Events

Hydrocodes have been widely used to study explosive events. A hydrocode is a type of program that numerically solves problems using conservation of mass, momentum and energy [53]. Hydrocodes are able to handle large deformations, and strain rates, such as shock waves [53, 54].

Hydrocodes typically use composite models to describe a material. The composite models relate an equation of state (EOS) that describes the unreacted material properties and an EOS that describes the reaction product properties [55]. An equation of state is used to relate the pressure, volume and temperature within a material [53]. The composite model ties the two EOSs together

with a burn rate. The burn rate is a homogeneous rate that is a simplification of the burn rate produced by the average burning rate due to hot spots in a particular explosive [55, 56]. Explosives are highly variable with different densities and microstructure depending on the method of manufacture. Due to this high variability in explosive microscale properties, the burn rates are calibrated to experimental data [55, 56].

These burn models are typically calibrated with shock-to-detonation experiments, such as the wedge test [55, 57]. The wedge test is usually conducted using a plane wave lens, attenuator and a wedge shaped explosive along with the imaging diagnostic equipment. Plane wave lenses are specially shaped explosives with the purpose of producing a planar detonation wave as opposed to the typical curved detonation front that is inherent in non-ideal explosives. A plane wave lens imparts a planar detonation wave into a driving explosive. The pressure is reduced to the desired level by the use of an attenuator. A known input pressure enters the wedge shaped explosive. The sloped surface of the wedge shaped explosive is mirrored. A light is shined on the sloped surface and is recorded by a streak camera. As the explosive reacts to the input pressure, the surface of the explosive at the burn/detonation front distorts the light. This distortion in light is recorded by the streak camera, and from a position versus time plot the velocity of the reaction can be calculated. When detonation is reached within the wedge explosive the reaction rate rapidly increases. The distance from the attenuator-wedge-shaped-explosive interface to the point of rapid velocity increase is referred to as the run distance [58].

Hydrocodes can provide a better understanding of unexpected phenomena occurring in experiments [53, 59]. Simulations may be conducted before expensive experiments to develop a better experimental matrix. Also in the case of limited funding, simulations could be used in place of experiments [53].

1.7 Goals of this Research

The goal of this research is to understand the effect of the microcracking on the detonation failure of PETN. The research investigated detonation failure processes using experiments and simulations. The experiments implemented artificial gaps between two films similar in concept to various gap test methods discussed earlier, to determine the size of gap the detonation can propagate across. Refractive imaging was used in conjunction with image processing techniques to extract the position and velocity of the shock front of detonating PETN films. CTH was used to model the PETN films to observe the shock and reaction product behavior.

CHAPTER 2

EXPERIMENTAL METHODS

Physical vapor deposition (PVD) was used to deposit PETN onto polycarbonate substrates using a deposition system at Sandia National Laboratories that utilized an effusion cell thermal deposition source. Films with thicknesses of 70 μm, 200 μm, and 400 μm were deposited. The thickness of the films was measured with a DektakXT surface profilometer with a 5 μm stylus. The 200 and 400 μm-thick films were deposited onto a polycarbonate substrate and were unconfined.

The 70 μm-thick films were deposited on polycarbonate substrates that were coated with a 1 μm-thick aluminum layer using e-beam deposition. There are two separate methods for the deposition of the aluminum substrate layer, which will be referred to as "bare aluminum" and "oxidized aluminum". The bare aluminum substrates were developed by coating a 1 μm-thick aluminum layer and without breaking vacuum, depositing a PETN layer. This substrate is referred to as bare aluminum since the aluminum does not have a chance to develop a significant amount of oxidation or contamination thus resulting in a high surface energy. The oxidized aluminum substrates were fabricated by coating a 1 μm thick aluminum layer followed by the removal of the substrate from vacuum. The substrate was placed under atmospheric conditions for approximately 24 hour to allow the aluminum to develop an oxide and contaminant layer. The substrates were then returned to vacuum for deposition of the PETN layer. The PETN was confined with a 1 μm-thick aluminum layer while under vacuum for both the bare and oxidized aluminum substrates [40].

The bare aluminum substrates are expected to have a significantly higher surface energy than the oxidized aluminum substrates. However an exact value for the surface energy is unknown since contact angle measurements were not able to be measured under vacuum. The theoretical surface energy for pure aluminum under a perfect vacuum is approximately 1140 mJ/m^2 [40, 60, 61]. The films were deposited at a base pressure of 1 x 10^{-6} Torr thus there was a small amount of contaminants present, lowering the surface energy of the aluminum [40]. Contact angle measurements were performed on the oxidized aluminum substrates resulting in a surface energy of approximately 40 mJ/m^2 [40]. Although the exact value of the surface energy of the bare aluminum used is unknown it is likely close to theoretical since deposition occurred under high vacuum.

Knepper et al. found that the PETN films deposited on oxidized aluminum substrates were thicker than the PETN films deposited on bare aluminum despite using the same amount of PETN for both substrate types. Thus it can be inferred that the PETN films deposited on bare aluminum are denser than the films deposited on oxidized aluminum. They also found that the detonation velocity of the PETN films deposited on bare aluminum was higher than the PETN films deposited on oxidized aluminum. This is the expected result for the respective densities of the films [40].

2.1 PETN Detonation Testing

The tests performed included steady-state detonation measurements through continuous films, detonation propagation and failure test with varied gap widths, and infinite gap width tests to measure the shock propagation through air from the end of the films. The detonation of the initial film in each setup was initiated by an incident shock from a detonating PVD PETN film directly above a small portion of the initial film.

The steady-state detonation tests consisted of a single PETN film deposited onto a 3 cm x 1 cm substrate as shown in Fig. 2.1. The 3 cm length provides sufficient distance for the detonation to reach and maintain steady-state throughout the length of the films. The purpose of this test configuration provides several frames of imaging at steady-state.

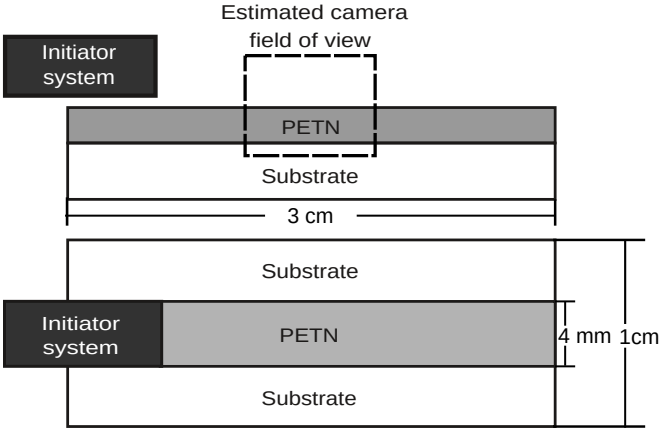

Figure 2.1: Schematic of the continuous film test setup. Included in the schematic is a rough estimate of the camera field of view.

There was also an implementation of a gap test to test the ability of detonation to propagate across a crack in the film, two films were placed next to each

other and physically separated by an air gap of known width as shown in Fig. 2.2. The films used in this arrangement were deposited onto individual 1 cm by 1 cm substrates. The size of the substrate and location of the initiator are chosen to provide enough length for the detonation to reach steady-state before entering the view of the camera and interacting with the gap.

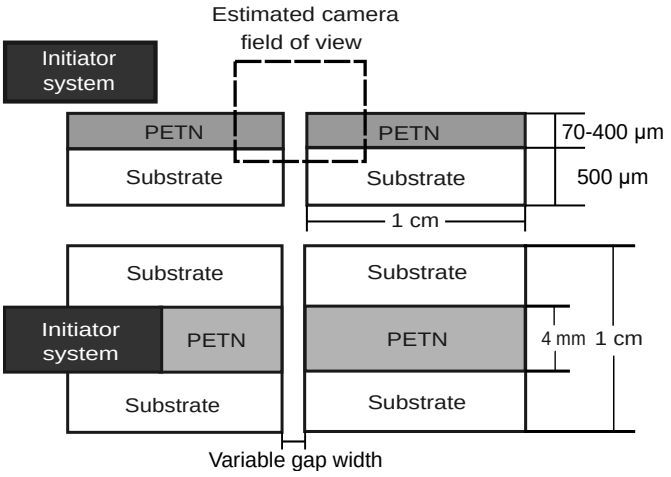

Figure 2.2: Schematic of the gap test setup. Included in the schematic is a rough estimate of the camera field of view.

The infinite gap test visualized the propagation of the air shock off the end of the film into free air as shown in Fig. 2.3. The test was performed to provide further insight to the gap tests. This test allowed for the visualization of the air shock formation inside the gap, before the air shock reaches the second film.

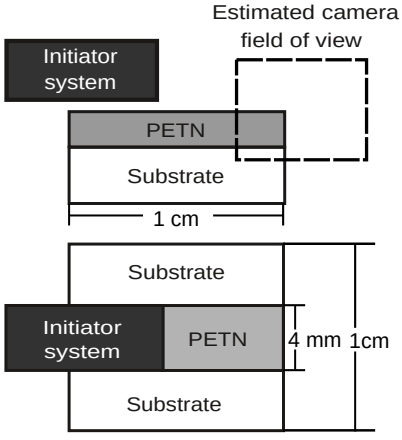

Figure 2.3: Schematic of the infinite gap test setup. Included in the schematic is a rough estimate of the camera field of view.

2.2 Refractive Imaging

Typical refractive imaging is done at medium to large scales with field of views ranging from centimeters in schlieren imaging to meters in retroreflective shadowgraph and background oriented schlieren [43]. To study the PETN films it was required that the horizontal field of view of the images be only few millimeters wide. This presents several issues with schlieren and focused shadowgraph. The first issue is that in order to avoid motion blur of an extremely fast moving object, i.e. a detonation front in a small field of view, a small exposure time is needed which reduces the amount of time light is collected. Therefore, a substantial amount of light is needed. Collecting a substantial amount of light in the required field of view has its issues and a balance needs to be struck. Schlieren and shadowgraph require the light passing through the imaging section to be highly parallel. Completely parallel light is impossible to achieve with a light source of finite size [43, 62], hence in refractive imaging it is desired to have the smallest divergence angle of the collimated light as possible. Fig. 1.2 is a schematic of the focused shadowgraph system used here. The divergence angle, θ, is dependent upon the focal length, f, of the collimating lens and the radius of the light source, r, as shown in eq. 2.1 [63, 62]. From this it is evident that in order to minimize the divergence angle, the radius of the light source needs to be minimized and the focal length needs to be maximized. The issue with this approach is that minimizing the light source radius and maximizing the focal length also minimize the light collected by the collimating lens. This is counterproductive to the goal of maximum light. Therefore it is desired to use a lens with the smallest focal length that gives a divergence angle that is deemed negligible to maximize light without sacrificing the accuracy of the imaging . This maximum acceptable divergence angle was determined here experimentally by utilizing a lens that would not produce a measurable change in radius of the collimated light through the length of the test section.

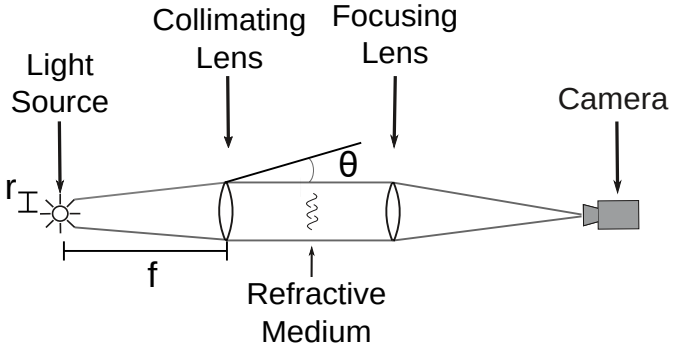

Figure 2.4: Shadowgraph system

$$\theta = \frac{r}{f} \tag{2.1}$$

The size of the light source in a schlieren system relative to the collimating lens also affects the blurring of schlieren objects. The smaller the light source is the crisper the schlieren object is. When the light source increases in size relative to the collimating lens the schlieren effect becomes more pronounced and results in a larger gradient. Fig. 2.5 shows the difference between images illuminated by a small light emitting diode (LED) and a large LED.

The data collected here were from two separate test series. Each test series was performed with slightly different optics as the optical system was incrementally improved. The optics in the second test series were slightly different in order to improve on the images from the first test series. The imaging method of the first test series will be discussed and then a discussion of the reasons for changing the setup on the second test series will follow. The imaging setup for test series 1 is shown in Fig. 2.6. The camera used was a Specialised Imaging SIMX-15. This camera is capable of recording 15 full resolution images at a frame rate of up to 1 billion frames per second. The camera uses a beam splitter to direct the light to its 15 individual image sensors to achieve such a high frame rate. Although each sensor can be triggered independently to allow variable frame rate, a constant frame rate was used in each test. The SIMX-15 records each individual image at a resolution of 1280 x 960 pixels with a bit depth of 12, and outputs saved images at 16 bits. Depending of the test, frame rates ranged from 10 to 66.66 MHz. All the images were taken at an exposure of 10 ns to minimize motion blur.

A Specialized Imaging SI-LUX 640 was used as the light source for all of the testing. The SI-LUX 640 is a spoiled coherence laser that outputs light via a liquid light guide. The light exiting the 5-mm-diameter light guide is incoherent with a divergence half angle of approximately 27 degrees. The SI-LUX 640 is an excellent source of light because it is extremely bright, and produces light at 640 +/- 6 nm. Since the SI-LUX 640 is essentially monochromatic, a bandpass filter at 640 nm was used to remove nearly all the explosive luminance that could overexpose the image.

The camera gain was used to enhance the light input to the camera sensor through the use of the integral image intensifier. The camera gain used ranged from 4-5, with each gain level increasing the camera intensity by a factor of 2. This level of gain provided enough light input to the camera sensor for a fully exposed 8 bit image.

The first test series used focused shadowgraph for every test, except the final test of the series which was performed with schlieren. All of the lenses used were 50-mm-diameter lenses. The SI-LUX 640 liquid light guide was mounted on an optical rod. The light was collected by a 175-mm-focal-length plano-convex lens. The light is collimated by this lens and is then turned by a first surface mirror (due to space constraints). The collimated light passes over the test section and is then focused with a 300-mm-focal-length achromatic doublet lens with a 175-mm-focal-length plano-convex lens place behind. The light is focused to a point and passes through the 640 nm bandpass filter. Then the light enters the camera through a 300-mm Nikon imaging lens. The 300-mm achromatic doublet lens and 175-mm plano-convex lens combination is used to provide a $\sim$3.2 mm

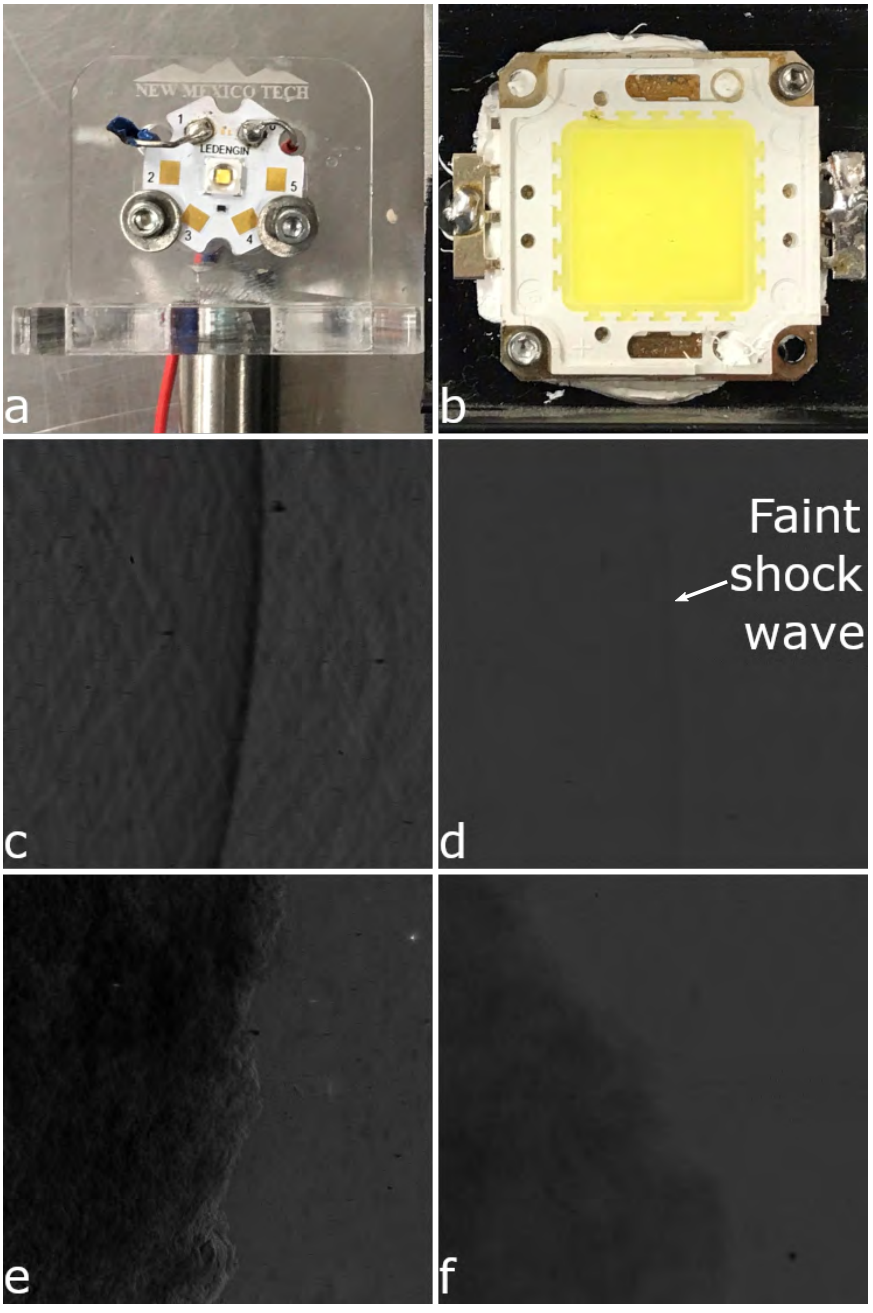

Figure 2.5: Schlieren imaging is performed with a (a) small and (b) large LED to produce the images (c-f). All images were taken with the same amount of light and with a 50% cutoff. Images (c) and (d) are of a shock wave and images (e) and (f) are of reaction product gases. The images in (c) and (e) used the small LED and images (d) and (f) used the large LED.

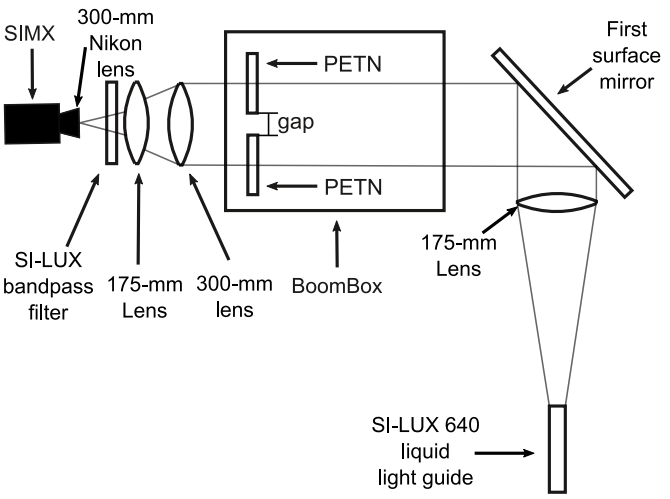

Figure 2.6: Schematic of the test series 1 imaging setup.

horizontal field of view when combined with the 300-mm Nikon imaging lens on the camera.

The final test of the series was performed with schlieren to explore whether additional flow features could be visualized. Schlieren imaging visualizes the first derivative of the refractive index field [43], and thus can have a higher sensitivity to weak refractive phenomena. Schlieren imaging was achieved by simply adding a knife edge directly in front of the camera, where the light is focused to a point. The imaging lens was also changed to give a $\sim$5.2 mm horizontal field of view. The larger field of view captured more light to make up for the light that was blocked by the knife edge. Approximately a 25% knife edge cutoff was used to provide a reasonable amount of sensitivity without losing too much light.

2.3 Test Series 2

After reviewing the images of the first test series it was observed that the schlieren imaging produced a crisper shock front than the focused shadowgraph imaging, which allowed for superior shock position data extraction. This led to the to use of schlieren for test series 2. Since larger aperture light sources tend to blur the shock front in schlieren images as discussed previously, a change was made to the collimating lens: the aperture of the light guide is fixed, so an alternative to changing the size of the light source is to change the focal length of the collimating lens. The collimating lens was changed from a 175-mm-focal length lens to a 200-mm-focal-length lens, effectively decreasing the size of the light source. Since the 200-mm focal-length lens does not capture as much light as the 175-mm-focal length lens, the field of view needed to increase to maintain sufficient light levels. A 200-mm Nikon lens was used to provide a larger

horizontal field of view of ≈5.2 mm. The cutoff was also reduced from a ≈25% cutoff to a 5-10% cutoff, since not much sensitivity was needed. A schematic of the optical system for test series 2 is shown in Fig. 2.7.

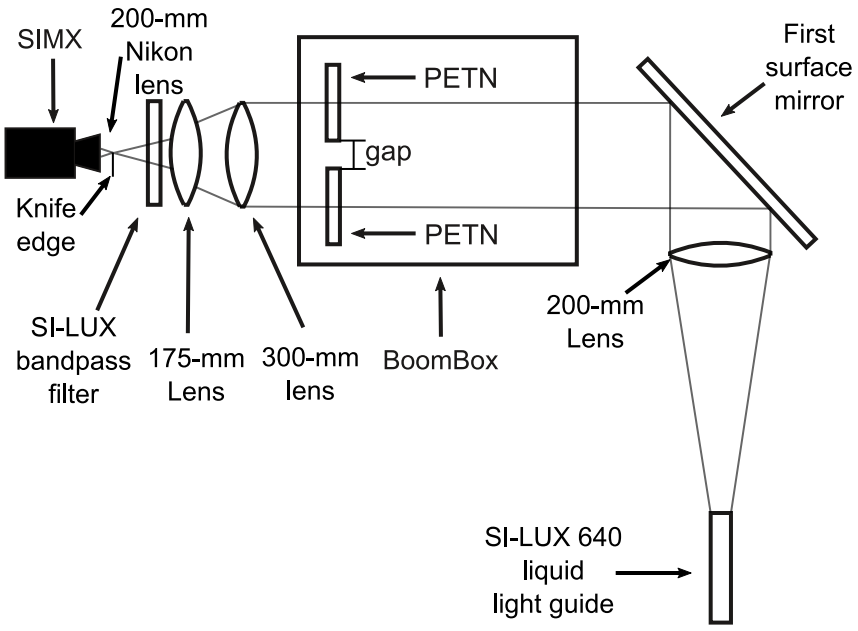

Figure 2.7: Schematic of the test series 2 imaging setup.

In test series 2 the gain on the camera was increased until the recorded image histogram comprised more than half of the bit depth. Since each successive step in camera gain increased the signal by a factor of 2, any further increase would result in an overexposed image. When using an underexposed image and stretching it, the intensity values are effectively binned into low counts, losing detail in the image. The histogram stretch effectively takes the pixel values saved at a low bit depth and places gaps between each value that stretch the values to the correct bit depth. The information in the gaps can never be recovered, due to it never being recorded in the first place. While the camera gain does add noise to the image, it is significantly better than a histogram stretch which also adds the same amount of noise. The advantage of camera gain is that increases the intensity of all the light before it is recorded by the camera thus utilizing the full bit depth of the camera sensor. Therefore detail that would have been lost due to the ”binning” that occurs with a histogram stretch is retained.

2.4 Image Processing

The SIMX-15 camera outputs 1 large image that is comprised of the 15 individual images it records. The large image is separated into the 15 individual

images for further processing. Since images are recorded at 12 bits and saved as 16 bits, a histogram stretch is performed on the images to stretch the histogram across the entire 16 bits of the image.

The Specialized Imaging software provided with the camera automatically rectifies the individual images between sensors using only x and y translations. An additional x and y translation, combined with a rotation image registration was applied using MATLAB to correct for slight errors in the Specialized Imaging software image registration.

A custom-developed image processing routine was built here to highlight the shock wave to automatically extract and measure the shape, spatial coordinates, and velocity. The general process is outlined here and shown in Fig. 2.8. The sequence is manually modified slightly between images to maximize the data extraction. First a Canny filter [64] was applied using the MATLAB *edge* function to create a binary image of the shock front. The Canny filter alone was sufficient for extracting the entire shock front in most images. In some images, gaps in connectivity of the Canny-filtered image were manually closed by inspecting the original image using the MATLAB *imfreehand* function, then merging the resultant image with the Canny-filtered image.

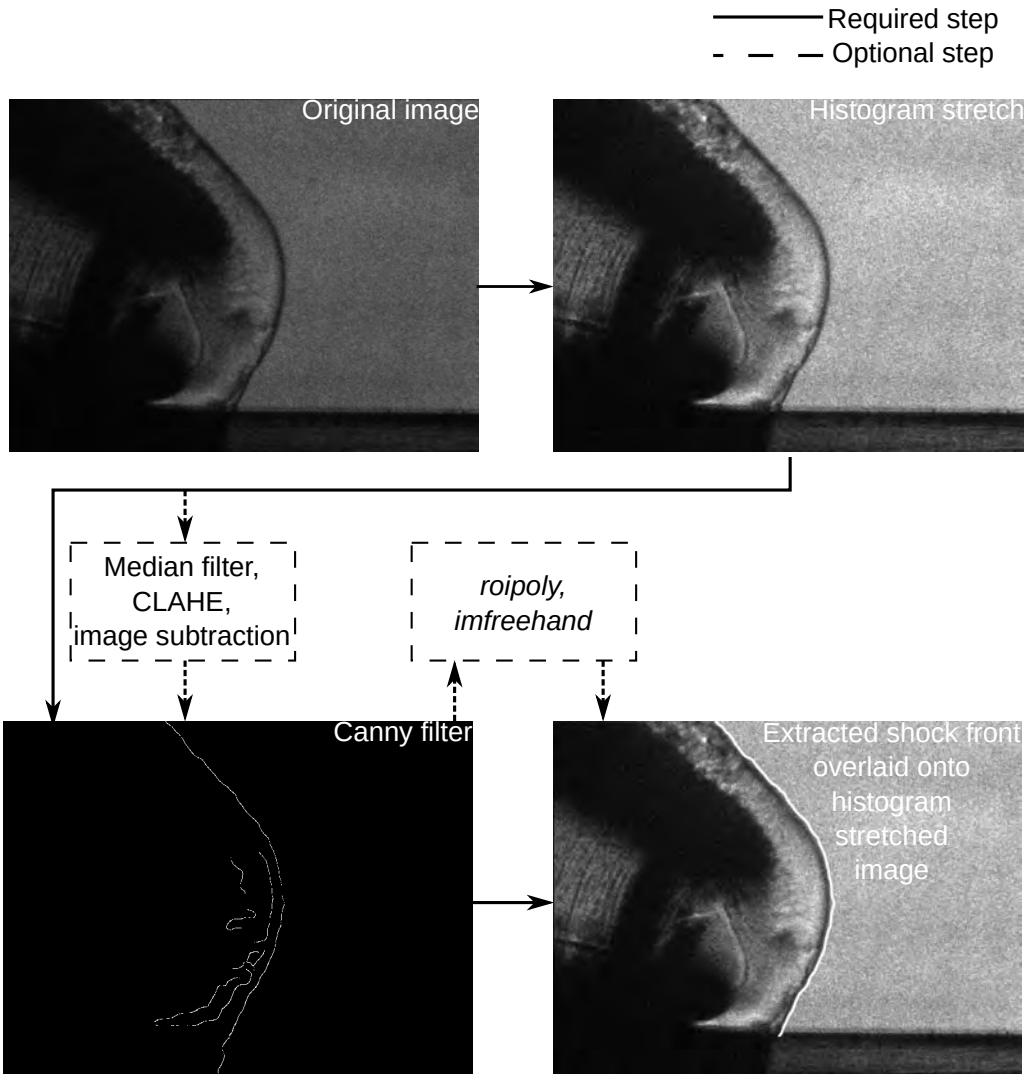

Figure 2.8: Image processing flow chart.

Small amounts of background noise due to low light levels were identified with the Canny filter. The noise was removed using the MATLAB *roipoly* function to create a mask for the background downstream of the shock wave location, which was then subtracted from the Canny-filtered image. Some images were enhanced prior to the Canny filtering using techniques including: median filtering, contrast limited adaptive histogram equalization [65], and static image subtraction. These techniques were applied to provide contrast between the shock front and the background.

Ultimately, the processing approach resulted in a binary image with the shock front location identified as a connected line of white pixels on a black background. The pixel coordinates of the shock front for each row in the image was extracted from the binary image. The pixel coordinates were converted to spatial coordinates using a calibration image of a grid with known spacing recorded

before the test.

2.5 Velocity Measurements

The velocity of the shock wave is calculated from the spatial coordinates in successive frames using a forward difference method [66]. A forward difference was chosen to provide the best resolution of the shock wave velocity change across the gaps between films. If a centered difference was used, the shock velocity upstream of the gap is affected by the velocity decay across the gap. When appropriate, centered differences were utilized for steady-state shock wave propagation.

The initial method to determine the velocity of the shock wave used a horizontal velocity calculation. This was achieved by comparing the shock wave position between points on the same pixel row. Since a shock wave is driven by pressure, it will always be traveling in the direction normal to the wave itself. The use of a horizontal velocity method is acceptable to measure the velocity of a steady-state detonation since the angle of the shock wave is consistent. The velocity of the shock wave normal to itself can be calculated through the application of a simple trigonometry calculation to the horizontal velocity of the wave. However, it fails to provide an accurate representation of what is occurring when the shock wave changes shape between frames during the unsteady detonation that occurs during the gap test. This is because the direction the shock wave is moving is variable along the shock front, and the trigonometric calculation is no longer applicable.

An appropriate method for calculating the velocity with unsteady wave shapes is to use a normal velocity method. In this method the velocity of the shockwave is always calculated in the direction of flow, which is the true motion of the shock wave itself. This method allows for the calculation of steady and unsteady flows.

The normal velocity calculation is completed using multiple steps as shown in Fig. 2.9. First the initial shock front, SF_1 is discretized into many small sections, then a linear curve fit [66] is applied to each of these sections. The size of each section used here was 49 points. At the boundaries of the shock front, this section size was reduced to the minimum allowable size of 7 points for a curve fit was reached. The size of 49 was chosen to provide plenty of points to reduce the effect of slight variances along the shock front, while still capturing the local shape. A derivative is taken of the curve fit equation at the center point to find the slope, m, of the curve fit. The first slope of interest, slope 1, is the slope of the line normal to the curve fit, m_n, and is calculated using eq. 2.2. All the points normal to the shock front at that location are then plotted to visualize the direction normal to the curve fit. A second slope, slope 2, is calculated between the center of the curve fit and each point on the subsequent shock front, SF_2. The difference, diff, is calculated between slope 1 and each slope 2. The differences are then split

up into differences that have a positive value and differences that have a negative value. The minimum of the positive differences and the negative differences are calculated. The points on SF_2 corresponding to the minimum of the positive difference and negative difference are the upper and lower bounds respectively. Due to the finite resolution of the points on the second shock front, SF_2, an exact match is highly unlikely. Therefore the point that is normal to the discretized section of the first shock front, SF_1, is known to lie somewhere between the upper and lower bounds.

$$m\_n = \frac{-1}{m} \tag{2.2}$$

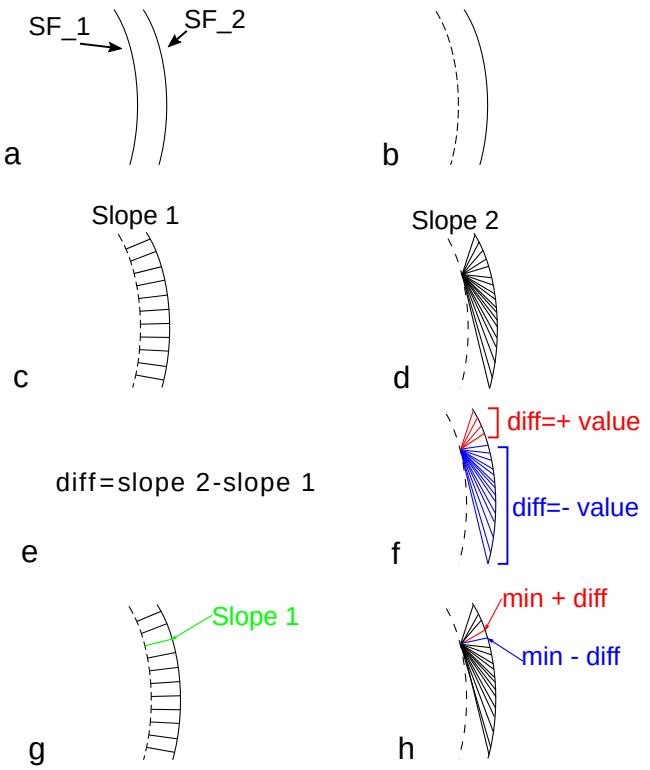

Figure 2.9: Normal velocity routine. a) Shock front data. b) Discretization of the first shock front, SF_1. c) A linear curve fit was performed for each discrete section of SF_1. The lines normal to the curve fit at each discrete section are found using the normal slope (Slope 1). d) Calculation of the slope (Slope 2) between the center of a discrete section and every point on the second shock front. This is processes is repeated for every discrete section. e) The difference between Slope 1 and every Slope 2 for a single discrete section is calculated. f) The lines corresponding to the Slope 2 are separated into difference values that are either positive or negative. g) The Slope 1 of interest. h) The points on SF_2 corresponding to the minimum of the positive differences and the minimum of the negative differences are the upper and lower bounds for the point normal to the highlighted Slope 1 in Fig. 2.9g.

CHAPTER 3

COMPUTATIONAL METHODS

The PETN films were modeled with CTH, a Eulerian finite difference hydrocode developed by Sandia National Laboratories. CTH modeling of the PETN films was performed to gain a better understanding of what is happening in the experimental images, and to understand the behavior of the reaction products.

3.1 Model Setup

The 2-dimensional model shown, in Fig. 3.1, consisted of two slabs of 200 μm-thick PETN films setup in the same configuration as the experimental gap test shown, in Fig. 2.2, along with a small initiator charge of PETN. An initiator charge of PETN is needed to initiate the initial PETN slab.

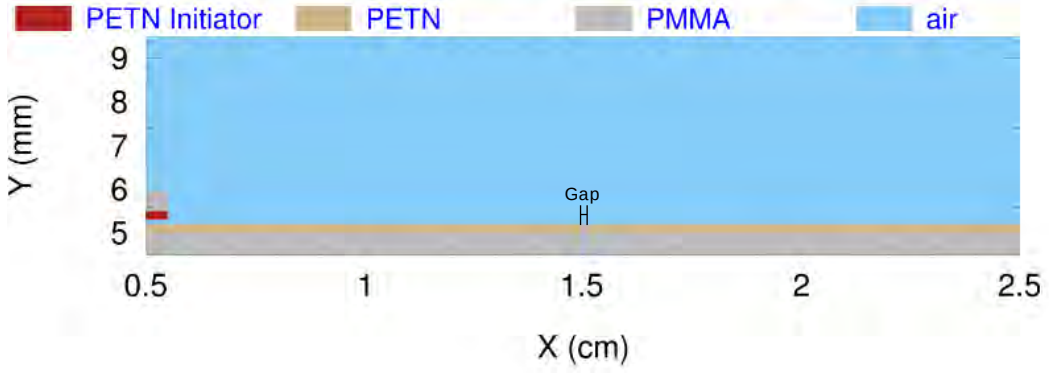

Figure 3.1: CTH model setup with the location of the gap shown.

The initiator charge was modeled with the Jones-Wilkins-Lee (JWL) [67] equation of state (EOS), which allows the use of a programmed burn initiation. The programmed burn propagates a detonation wave from a point that expands radially [68]. The JWL EOS only describes the gaseous reaction products, which is suitable for the initiator but not for modeling PETN films of interest.

The initial PETN film was initiated by an incident air shock from the initiation charge. The film was modeled with the HVRB reaction rate model [38].

An HVRB model was chosen as the reaction rate model for the PETN films due to its usefulness in representing shock initiation of explosives [38]. The HVRB model is a composite pressure dependent reactive burn model. HVRB is typically calibrated from the run distance to detonation versus input pressure results obtained from wedge test data [57]. Since the wedge test data used is from pressed explosives, the HVRB calibration does not allow for the initiation of PETN at a thickness of 200 μm. Thus a few adjustments were made to the reaction rate parameters of the HVRB model to allow for detonation of the 200 μm-thick films. The film was long enough for detonation to reach steady-state before the gap interface, thus the initiator had no effect on the results.

The HVRB model relates an equation of state model describing the solid unreacted phase of the explosive to another equation of state model that describes the gaseous reaction product state. The Mie Grüneisen EOS was used to describe the solid unreacted form of the explosive, while a Sesame tabular EOS [69] was used to describe the material in the gaseous reaction product state.

A polycarbonate EOS was not present in the CTH library. Thus a polymethyl methacrylate (PMMA) substrate was used in its place. The PMMA substrate was modeled with a Mie Grüneisen EOS. The air was modeled using a Sesame tabular EOS under standard temperature and pressure (STP) conditions.

CTH calculates all values such as the volume fraction of species, velocity, and density at the center of the cell [70]. Due to this it is desirable to use a square mesh since a non proportional rectangular mesh could cause errors. A standard mesh of cells with an aspect ratio of 1:1 was used to acquire the highest accuracy in all simulations. A mesh resolution of 8000 cells wide by 2000 cells high was used over the spatial domain of 2 cm wide by 0.5 cm high. This mesh size is too fine to show in full detail in a single image so Fig. 3.2 shows the mesh for an 80 x 20 cell grid scaled down with each cell representing a 100 x 100 mesh grid.

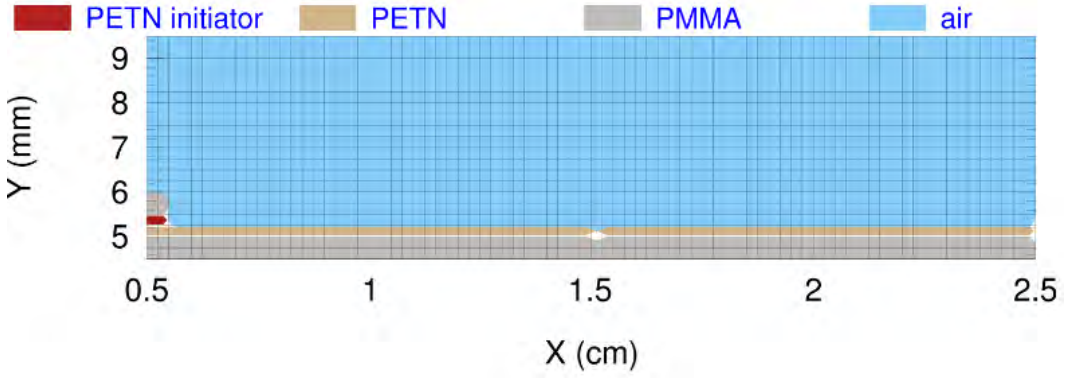

Figure 3.2: 80 cell wide by 20 cell high 2-dimensional model setup with a mesh grid overlay. Each cell represents a 100 by 100 cell grid in the actual 8000 by 2000 problem setup.

A transmitting boundary condition was used on all the boundaries. The

transmitting boundary condition allows mass to flow in and out of the mesh. Weak reflection of incident waves may occur with this type of boundary condition [38]. However the boundaries were far enough away from the region of interest to not affect the results here.

The mesh grid was chosen to have a similar spatial resolution of μm/cell as the μm/pixel resolution of the experimental images. The micrometer per cell ratio is 2.5 μm/cell, while the experimental micrometer per pixel ratio ranges from 2.57 to 3.89 μm/pixel. Images of the computational domain displaying density are exported as a primary data output of the simulations. The inter-frame time between image output from the simulation was 10 ns to provide a temporal resolution that exceeded all the experimental testing.

An infinite gap test was also performed by simply removing the second PETN film and its corresponding substrate.

3.2 Computer Generated Schlieren

Computer generated schlieren (CGS) images were made to visualize the shock wave and reaction products. As previously discussed, schlieren images are the first derivative of the refractive index field. Although CTH does not have a refractive index output, the refractive index, n, is proportional to density ρ: [43]

$$\rho = \frac{n-1}{k} \tag{3.1}$$

Where k is the Gladstone-Dale coefficient. From this relationship it is clear that the refractive index gradient is simply proportional to the density gradient, so the density gradient is used here to make schlieren images. The derivative can be taken by using a finite difference method [66]. Since a vertical cutoff was used in the experimental testing, the derivative was taken along the horizontal direction to produce an equivalent schlieren image. A centered difference method was chosen instead of a backward or forward difference to provide higher accuracy. The centered difference derivative can be calculated with a step size of h:

$$\frac{dx}{dy} = \frac{x_{n+h} - x_{n-h}}{2h} \tag{3.2}$$

The numerical derivative can be calculated using a simple image processing routine, called spatial filtering [71]. Spatial filtering is performed by applying a mask composed of multiplication factors, C_i, to a region of pixels. Fig. 3.3 shows the application of a mask to an image centered on pixel x_i,y_i. Each pixel covered by the mask is multiplied by the value in the mask that corresponds to

the location of the pixel. The filtered value of the centered pixel is equal to the sum of each pixel multiplied by their respective mask value and is given by:

$$\begin{aligned} \textit{Filtered cell value} = {} & C_1 * (x_{i-1}, y_{i+1}) + C_2 * (x_i, y_{i+1}) + C_3 * (x_{i+1}, y_{i+1}) \\ & + C_4 * (x_{i-1}, y_i) + C_5 * (x_i, y_i) + C_6 * (x_{i+1}, y_i) \\ & + C_7 * (x_{i-1}, y_{i-1}) + C_8 * (x_i, y_{i-1}) + C_9 * (x_{i+1}, y_{i-1}) \end{aligned} \quad (3.3)$$

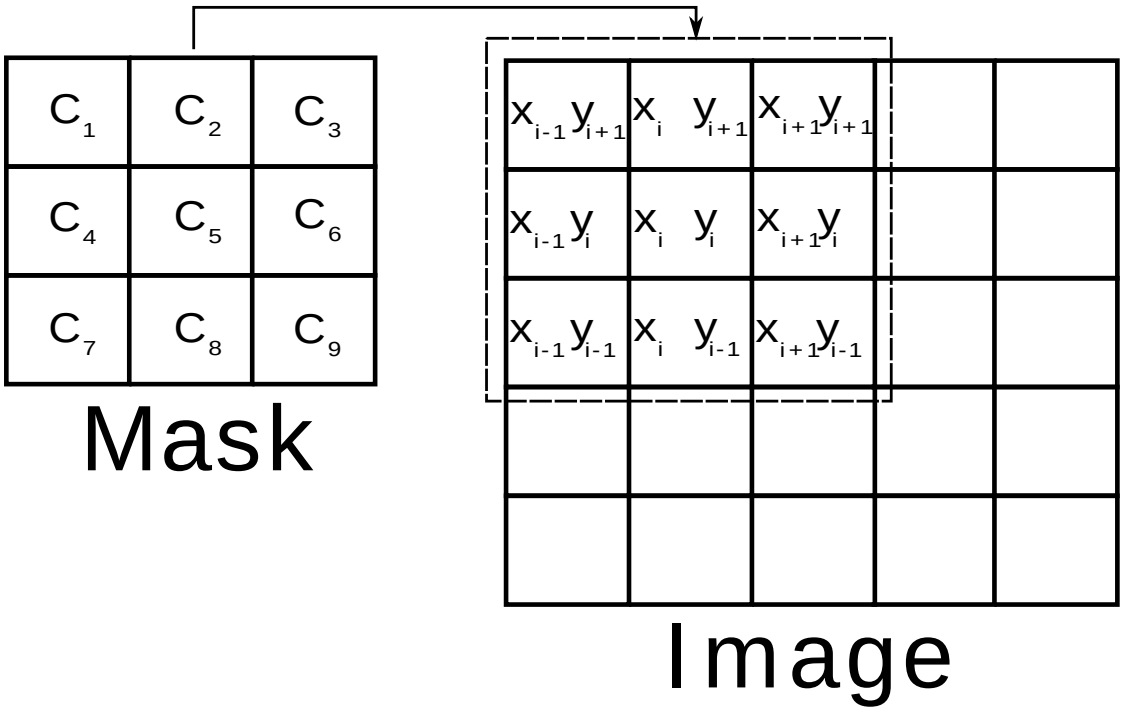

Figure 3.3: The mask composed of coefficients, C_i, is applied to the image centered on pixel x_i,y_i.

A custom edge detection mask, which is similar to a Prewitt filter [71] was used to take the numerical horizontal derivative. The custom mask is a 3 cell wide by 1 cell high filter instead of the 3 cell wide by 3 cell high Prewitt filter. The 3x1 configuration was chosen to localize the schlieren effects to a single cell row. The custom kernel shown, in Fig. 3.4, put into equation form with the notation of x for each cell, yields:

$$\textit{Filtered cell value} = -1 * x_{n-1} + 0 * x_n + 1 * x_{n+1} \qquad = x_{n+1} - x_{n-1} \quad (3.4)$$

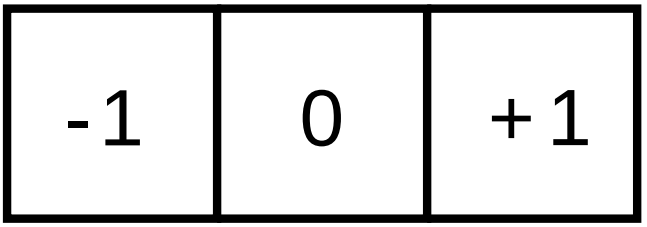

Figure 3.4: Custom schlieren mask.

Synthetic schlieren allows for the visualization of the shock wave and reaction products in a manner similar to actual schlieren imaging. Only a small portion of the image was visualized with synthetic schlieren as shown, in Fig. 3.5, to mimic the imaging field of view used during experimental testing. The vertical height of the model was much larger than the imaged field of view so boundary effects would not be captured in the imaged field of view.

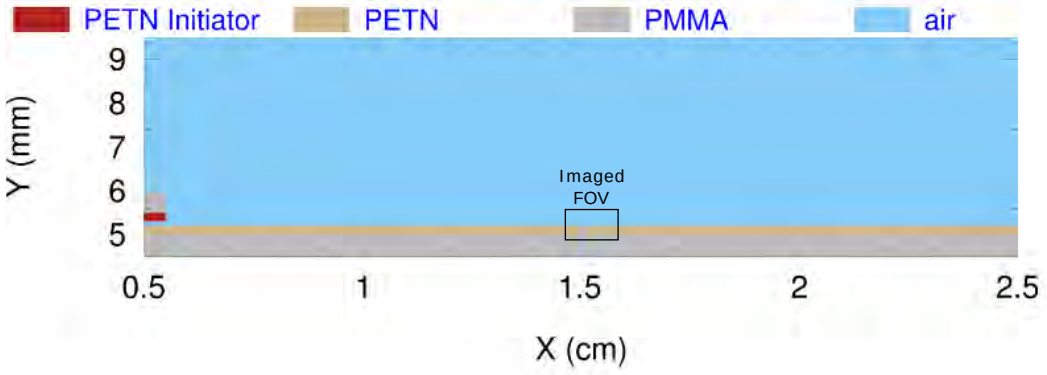

Figure 3.5: CTH model setup. The field of view (FOV) of the computer generated schlieren images is shown.

3.3 Velocity Measurement of Computer Generated Schlieren Images

The normal velocity plots described in section 2.5, are created here from the CGS images. Results of the normal velocity plots can be compared between the experimental and computational schlieren images. The inter-frame time between image output from the simulation was 1 ns. However, the normal velocity plots were only plotted at an inter-frame time of 10 ns to allow for the visualization of the full evolution of the shock front while keeping the plots relatively

uncluttered. Velocity data can be calculated between individual frames or is calculated across multiple frame to show the full evolution of the shock front while keeping the plots relatively uncluttered.

A Canny filter was not necessary to highlight the shock front of the CGS image. Since camera sensor noise was not present, a simple binarization of the image highlighted the shock front. The shock front location was extracted and the normal velocity plot procedure proceeded in the same way as discussed in Chapter 2.

CHAPTER 4

EXPERIMENTAL RESULTS

PETN films of thicknesses ranging from 70 to 400 μm-thick were evaluated. Table 4.1 list all the tests performed. The 200 and 400 μm-thick PETN films were deposited on polycarbonate substrates and were unconfined. The 70 μm-thick PETN films were confined with aluminum and deposited onto bare and oxidized aluminum coated polycarbonate substrates.

Table 4.1: Test matrix table.

Test #	Film Thickness (μm)	Inter Frame Time ΔT (ns)	Gap Width (μm)	Horizontal Field of View (mm)	Substrate
1	70	60	Continuous	4.914	Oxidized aluminum
2	70	60	Continuous	4.914	Bare aluminum
3	70	60	0	4.914	Oxidized aluminum
4	70	60	0	4.914	Bare aluminum
5	70	60	10	4.914	Oxidized aluminum
6	70	60	10	4.914	Bare aluminum
7	70	60	25	4.914	Oxidized aluminum
8	70	60	25	4.914	Bare aluminum
9	70	60	50	4.914	Oxidized aluminum

Table 4.1: —continued

Test #	Film Thickness (μm)	Inter Frame Time ΔT (ns)	Gap Width (μm)	Horizontal Field of View (mm)	Substrate
10	70	60	50	4.914	Bare aluminum
11	70	35	Infinite	4.914	Oxidized aluminum
12	70	35	Infinite	4.914	Oxidized aluminum
13	70	60	Infinite	4.914	Oxidized aluminum
14	70	35	Infinite	4.914	Bare aluminum
15	70	60	Infinite	4.914	Bare aluminum
16	200	60	Continuous	N/A	Polycarbonate
17	200	60	Continuous	N/A	Polycarbonate
18	200	90	Continuous	N/A	Polycarbonate
19	200	90	Continuous	N/A	Polycarbonate
20	200	45	Continuous	3.286	Polycarbonate
21	200	60	Continuous	4.978	Polycarbonate
22	200	60	Continuous	4.914	Polycarbonate
23	200	60	25	N/A	Polycarbonate
24	200	60	25	N/A	Polycarbonate
25	200	90	25	N/A	Polycarbonate
26	200	100	25	3.286	Polycarbonate
27	200	45	25	3.286	Polycarbonate
28	200	60	50	N/A	Polycarbonate
29	200	50	50	3.286	Polycarbonate
30	200	60	75	N/A	Polycarbonate
31	200	90	75	N/A	Polycarbonate
32	200	45	80	3.286	Polycarbonate
33	200	45	˜75-120	3.286	Polycarbonate
34	200	50	˜93	3.286	Polycarbonate
35	200	45	95	3.286	Polycarbonate
36	200	60	100	N/A	Polycarbonate
37	200	50	110	3.286	Polycarbonate
38	200	45	110	3.286	Polycarbonate

Table 4.1: —continued

Test #	Film Thickness (μm)	Inter Frame Time ΔT (ns)	Gap Width (μm)	Horizontal Field of View (mm)	Substrate
39	200	45	170	3.286	Polycarbonate
40	200	60	Infinite	N/A	Polycarbonate
41	200	60	Infinite	N/A	Polycarbonate
42	200	90	Infinite	N/A	Polycarbonate
43	200	45	Infinite	3.286	Polycarbonate
44	200	15	Infinite	3.286	Polycarbonate
45	400	60	80	4.914	Polycarbonate
46	400	60	100	4.914	Polycarbonate
47	400	60	125	4.914	Polycarbonate
48	400	60	160	4.914	Polycarbonate
49	400	60	180	4.914	Polycarbonate
50	400	60	180	4.914	Polycarbonate
51	400	60	200	4.914	Polycarbonate
52	400	60	200	4.914	Polycarbonate
53	400	60	220	4.914	Polycarbonate

4.1 Continuous Film Test

The image sets in Fig. 4.1 and Fig. 4.2 display a shock front produced by confined PETN films deposited on bare and oxidized aluminum substrates respectively. These films both produced a shock front that is non-uniform. The shock front appears to be several Mach stems that stack on top of each other. The structures that appear to be Mach stems eventually coalesce into a singular shock front. Since these films are 70 μm-thick, they are close to the critical thickness for films of this configuration which is approximately 55 μm [40]. The shock shape could be caused by porosity within the microstructure, which would not be noticeable in thicker films due to the bulk effects dominating. This effect is similar to Ramsay and Popolato's findings of a rough shock front caused by small local discontinuities in explosives [72].

The 70 μm-thick PETN film deposited on the substrate coated with bare aluminum, shown, in Fig. 4.1, appears to have a rougher shock front shape than the 70 μm-thick film deposited on a substrate coated with oxidized aluminum, as shown in Fig. 4.2.

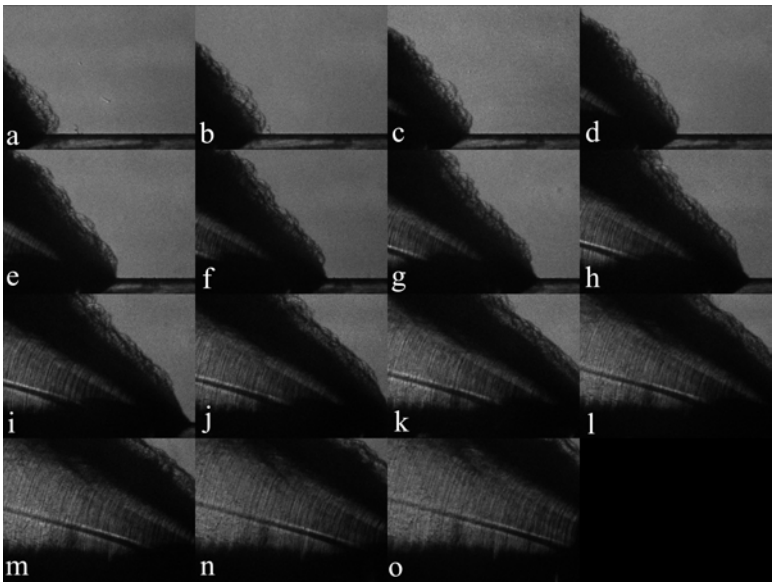

Figure 4.1: Schlieren images from Test 2 arranged from left to right then down. Test 2 is a continuous film detonation test of a 70 μm-thick aluminum confined PETN film deposited onto a bare aluminum substrate.

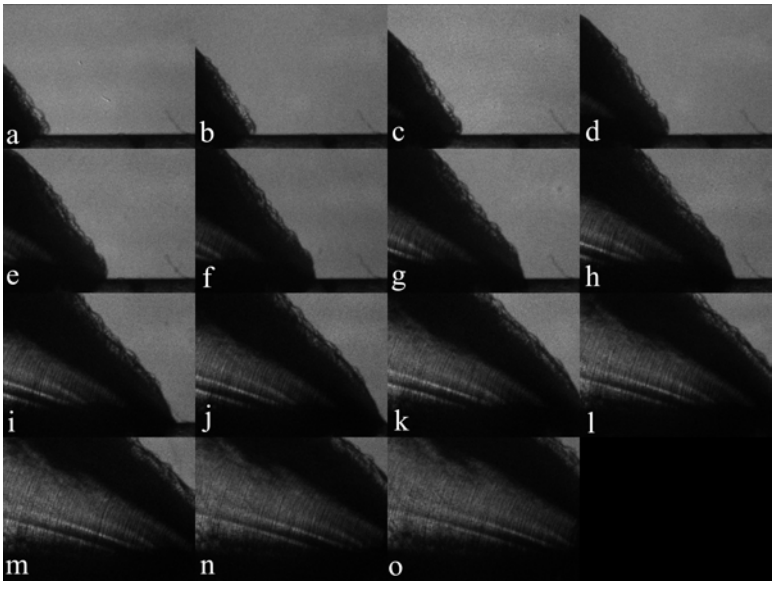

Figure 4.2: Schlieren images from Test 1 arranged from left to right then down. Test 1 is a continuous film detonation test of a 70 μm-thick aluminum confined PETN film deposited onto a oxidized aluminum substrate.

Normal velocity plots were made to visualize velocity of the shock front as the shock passed through the field of view of the camera. The highlighted

shock fronts for each frame in the sequence were plotted in black. In addition the normal velocity vectors calculated as described in Chapter 2 are plotted and color coded to specify velocity. Normal velocity vectors that have a velocity uncertainty due to slope matching greater than $\pm$ 50 m/s are rejected. Although the velocity values that don't meet the uncertainty requirement are not included in the analysis, they are plotted in black to verify which vectors were excluded.

The normal velocity plot for a 70 μm-thick aluminum confined PETN film deposited on bare aluminum, shown, in Fig. 4.3, displays some vectors that are clearly not in the direction of the shock motion. This is not an error in the curve fitting as the vectors are correctly pointing in the direction normal to the shock front. It is due to the highly irregular shape of the shock front. Nevertheless, it can be seen that as the detonation transitions to steady-state the velocity increases and the shock front smooths out.

The normal velocity plot of the 70 μm-thick aluminum confined PETN film deposited on a substrate coated with oxidized aluminum in Fig. 4.4 has significantly less diverging vectors since the shock front is slightly smoother. The diverging vectors are present but hardly noticeable since the roughness of the shock front isn't great enough to cause a significant velocity spike. It can also be seen that the velocity of the shock front increases significantly as the detonation reaches steady-state.

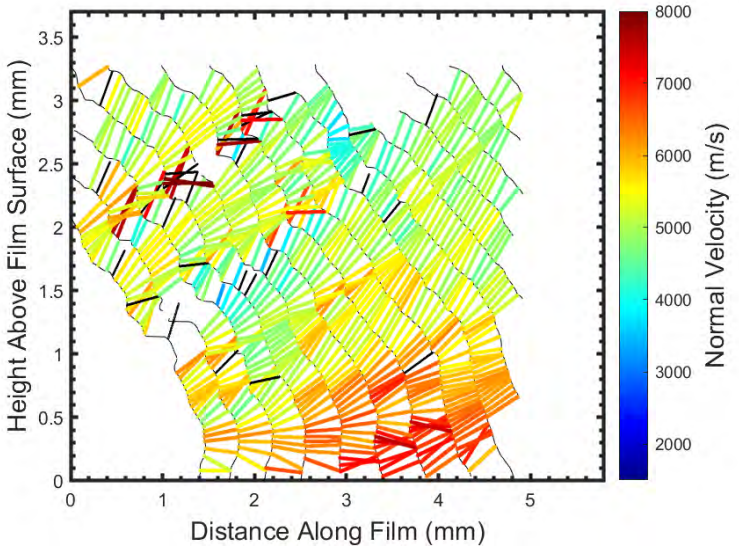

Figure 4.3: Normal velocity plot of Test 2. The tracked shock fronts from test 2 were plotted as thin black lines. The black vectors represent vectors that did not meet the desired shock front matching uncertainty criteria.

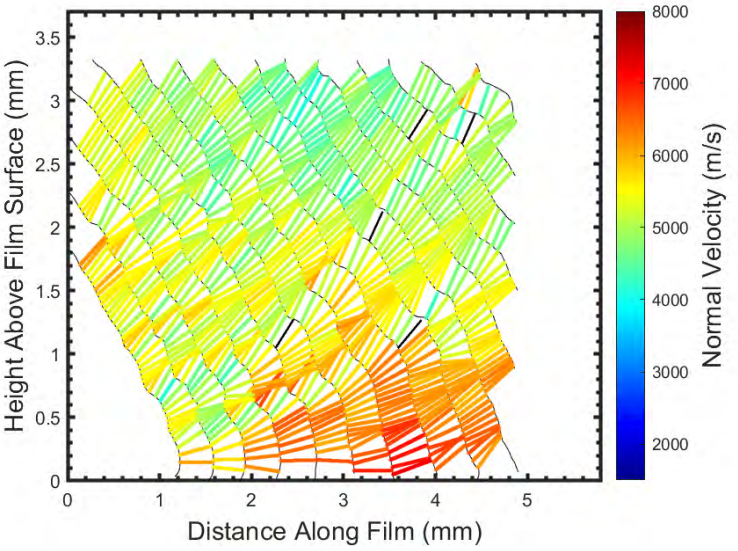

Figure 4.4: Normal velocity plot of Test 1. The tracked shock fronts from test 1 were plotted as thin black lines. The black vectors represent vectors that did not meet the desired shock front matching uncertainty criteria.

The 200 μm-thick films reach steady-state before entering the imaged field of view as shown in Fig. 4.5. It is believed that the 200 μm-thick unconfined PETN films reach steady-state earlier than the 70 μm-thick aluminum confined PETN films, however it is not confirmed due to an inconsistent horizontal alignment of the films within the camera field of view.

The normal velocity plot of the 200 μm-thick PETN film in Fig. 4.6 shows that the velocity of the shock front remains relatively steady across the entire field of view. The 200 μm-thick PETN films could be thick enough for bulk properties to start having a greater effect rendering the microstructural effects causing the rough shock front to be negligible.

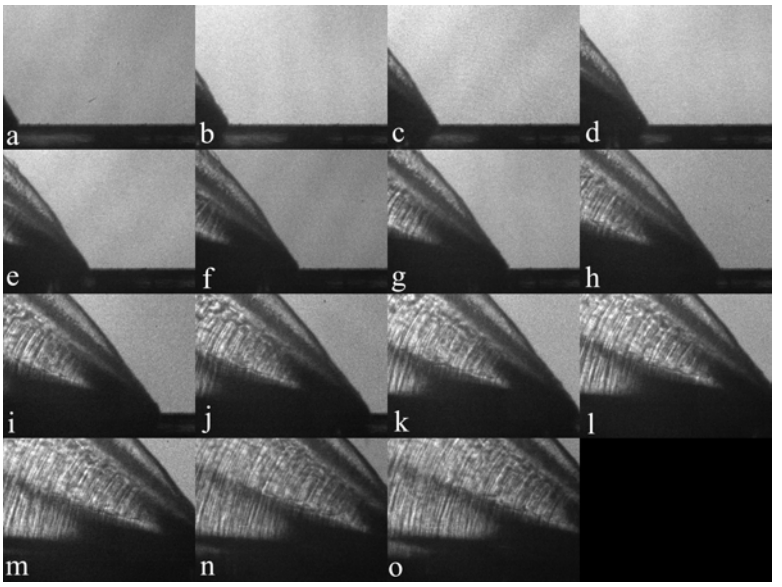

Figure 4.5: Schlieren images from Test 21 arranged from left to right then down. Test 21 is a continuous film detonation test of a 200 μm-thick unconfined PETN film.

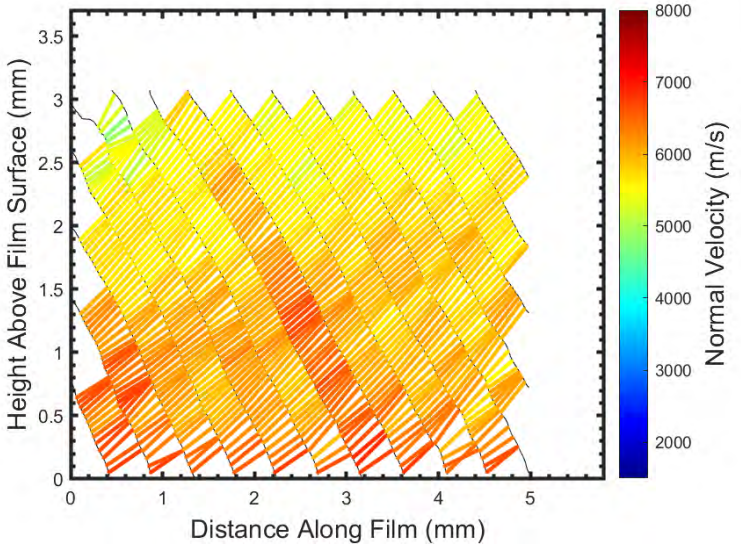

Figure 4.6: Normal velocity plot of Test 21. The tracked shock fronts from Test 21 were plotted as thin black lines.

The detonation velocity of select continuous film tests was calculated by measuring the velocity of the air shock along the film surface. The calculation of the detonation velocity was performed by manually clicking on the shock front

along the edge of the film on successive frames to obtain position versus time data. The frames used for the velocity calculations were all at steady-state. This allowed for the use of a centered difference calculation, which provides higher accuracy. The velocity calculation was centered on three separate frames for three calculations in each test. Each calculation was repeated three times and the average of the 9 values was reported in Table 4.2. The uncertainty was found by taking the standard deviation of the 9 calculations for each test.

In order to validate photometric measurements, detonation velocity of the 200 μm-thick films was also measured with a fiber probe lid similar to the method discussed in [22]. The fiber probe velocity measurements are within 1% of the well accepted method of streak camera analysis data [22]. The fiber probe lid is a polycarbonate lid with 7 optical fibers placed into laser machined holes. The holes are along the center of the film width and are spaced at an interval of 3.5 mm along the film length. The lids are attached to the fixture and do not confine the PETN films. The light from the detonation is recorded with a digital storage oscilloscope. As the detonation reaches each fiber, a peak in intensity is recorded by the oscilloscope. A linear least squares curve fit is applied to the time versus position data of the peaks, which yields a slope that is equal to the detonation velocity. The uncertainty reported is calculated by the standard error of the estimate [73]

Test "Fiber Probe 1" has ideal results, with distinct peaks as shown in Fig. 4.7. Test "Fiber Probe 2" had rough peaks as shown in Fig. 4.8, which was the likely cause of the high uncertainty seen in Table 4.2. There is general agreement between the shock front and fiber probe lid data of the 200 μm-thick films. The variation between the velocity results is within the measurement uncertainty.

Table 4.2: Detonation velocity table.

Test #	Film Thickness (μm)	Detonation Velocity (m/s)	Substrate Material	Measurement
1	70	7450 ± 116	Oxidized Aluminum	Shock Front
2	70	7910 ± 53	Bare Aluminum	Shock Front
21	200	7651 ± 197	Polycarbonate	Shock Front
22	200	7513 ± 135	Polycarbonate	Shock Front
Fiber Probe 1	200	7536 ± 31	Polycarbonate	Fiber Probe Lid
Fiber Probe 2	200	7391 ± 251	Polycarbonate	Fiber Probe Lid

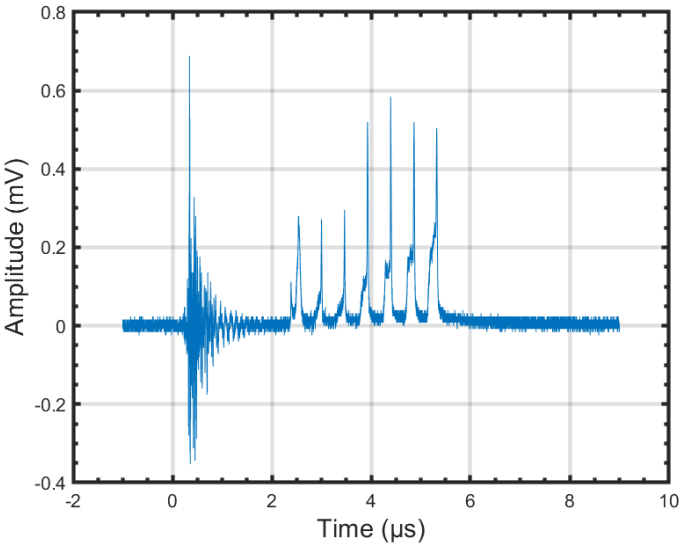

Figure 4.7: Oscilloscope data from Test ”Fiber Probe 1”. Each of the 7 peaks correspond to the time when the detonation light reached each fiber.

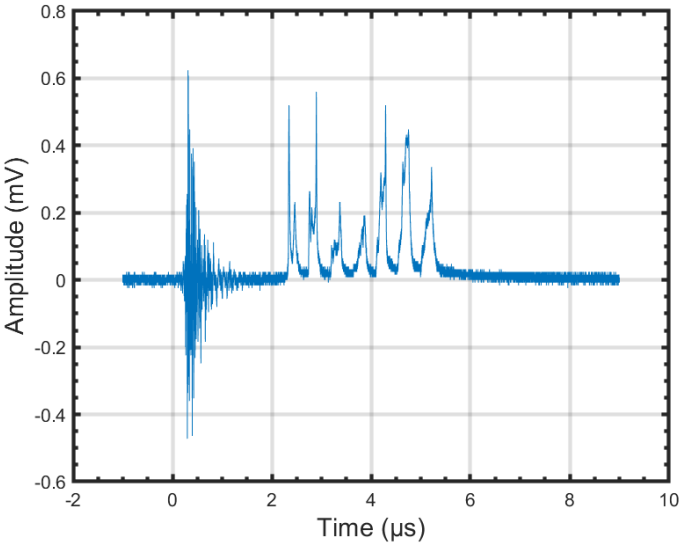

Figure 4.8: Oscilloscope data from ”Test Fiber Probe 2”. Each of the 7 peaks correspond to the time when the detonation light reached each fiber.

4.2 Gap Test

Gap tests were performed to measure the critical gap width. Due to difficulty in assembling the test articles, not every test had films that were perfectly

aligned in the vertical direction. It is important to know that the height above film surface measurement included in the normal velocity plots is measured from the lower of the two films.

The normal velocity plots used to analyze the shock front give a substantial amount of information. All the velocity plots for the gap tests have the same x and y axis limits to allow for easy comparison of tests regardless of the field of view or inter-frame time used.

The shock front changes shape and speeds up as the detonation crosses the gaps and re-establishes a steady-state propagation which can be easily observed in the normal velocity plots. The point at which the shock front speeds up is related to the run distance. The run distance is defined as the distance an input pressure needs to travel within an explosive to reach detonation. The exact run distance may not be be at the point where the shock wave speeds up and changes shape. This is because while the reaction is building up to detonation, there is a possibility that the air shock from the initial film is traveling at a faster rate than the developing reaction. If this is the case, after the detonation occurs the detonation front will need to catch up with the air shock before the air shock returns to its steady-state shock shape. Due to the uncertainty in location of the run distance in relation to the change in shock wave shape, the terminology for the distance to the change in wave shape will be referred to as the distance to steady-state wave shape.

4.2.1 Critical Gap Width

The critical gap width is the largest width of gap for reliable initiation of the second film. Table 4.3 shows the results for each gap test. None of the 70 μm-thick aluminum confined PETN films propagated across the narrowest 10 μm gaps. Therefore the 70 μm-thick films were placed in contact with each other to make as small of gap as possible. Neither of the 70 μm-thick films were able to propagate across this abutment gap. This was likely due to the fact that the films were close to their critical detonation thickness (55 μm) [40]. The 200 μm-thick unconfined PETN films had a critical gap width of about 80 μm. Although detonation was observed at a width beyond 80 μm, it was deemed unreliable due to a significant amount of failures above 80 μm. The 400 μm-thick unconfined PETN films had a critical gap width of approximately 180 μm. A limited number of tests were performed at this 400 μm thickness, with one of them failing to detonate across a gap width of 200 μm. The gap widths reported here have a general uncertainty of $\pm$ 10 μm due to edges that are slightly rough. Test 33 had an edge that was significantly rougher than other films and thus the range of widths is reported in Table 4.3.

Table 4.3: Test failure table

Test #	Film Thickness (μm)	Gap Width (μm)	Detonation Propagation
3	70	0	No
4	70	0	No
5	70	10	No
6	70	10	No
7	70	25	No
8	70	25	No
9	70	50	No
10	70	50	No
23	200	25	Yes
24	200	25	Yes
25	200	25	Yes
26	200	25	Yes
27	200	25	Yes
28	200	50	Yes
29	200	50	Yes
30	200	75	Yes
31	200	75	Yes
32	200	80	Yes
33	200	75-120	Yes
34	200	93	No
35	200	95	No
36	200	100	No
37	200	110	Yes
38	200	110	No
39	200	170	No
45	400	80	Yes
46	400	100	Yes
47	400	125	Yes
48	400	160	Yes
49	400	180	Yes
50	400	180	Yes
51	400	200	Yes
52	400	200	No
53	400	220	Yes

The criteria to determine whether or not a detonation successfully propagated across a gap was the shape of the shock front in the second film. The shock front develops a circular discontinuity shape and returns to its linear steady-state shape if the detonation successfully propagates across the gap as is shown in Fig. 4.9. If the detonation fails to propagate across a gap, the shock front becomes more circular as shown in Fig. 4.10.

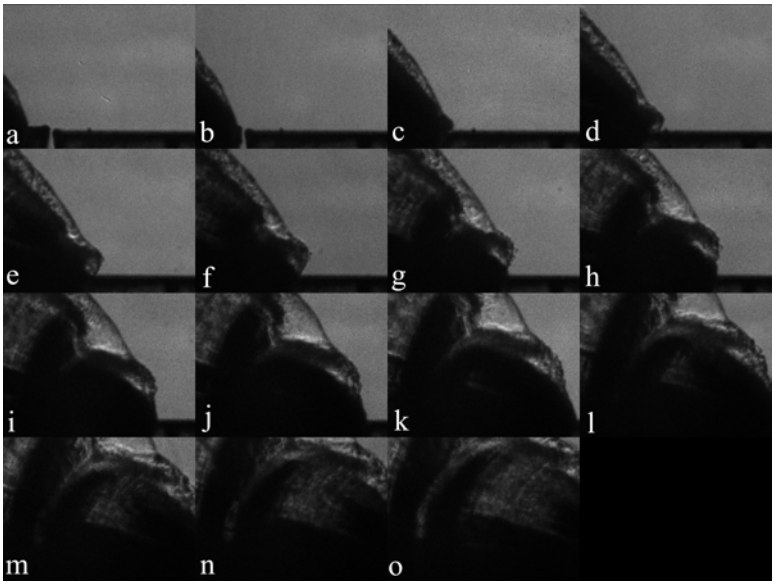

Figure 4.9: Detonation test sequence for a successful propagation in Test 46. The images are arranged from left to right then down.

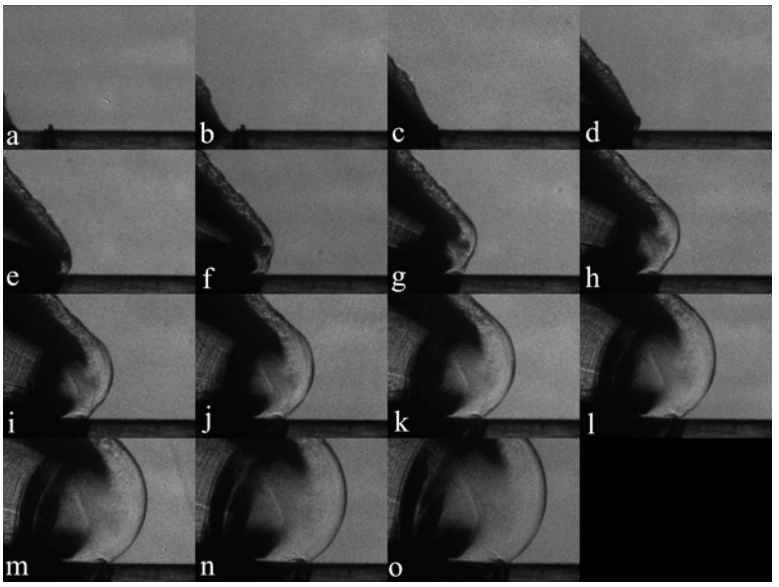

Figure 4.10: Detonation test sequence of an unsuccessful propagation in Test 10. The images are arranged from left to right then down.

The polycarbonate substrates upon which the PETN films were deposited on were collected after each test for examination. The substrates belonging to films that detonated were significantly bent inwards as shown in Fig. 4.11.

Figure 4.11: Test 32 dent track due to a successful initiation across the gap.

Not surprisingly, upon collection of the substrate belonging for a film that was shown to not detonate, it was observed that the substrate did not contain any residual PETN nor any significant deformation as shown in Fig. 4.12.

Therefore the post-test substrate provides a supplementary indication of successful/unsuccessful detonation propagation.

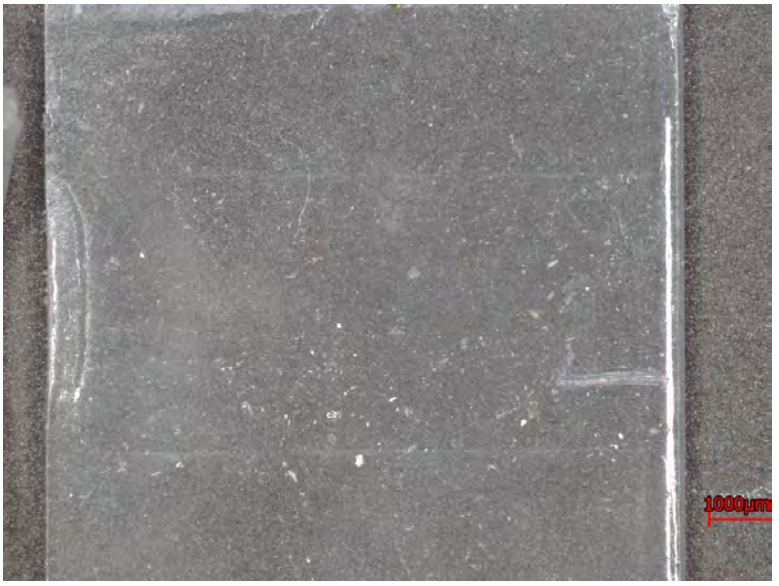

Figure 4.12: Test 38 flat substrate due to a failure to propagate across the gap.

4.2.2 Successful Initiation

Fig. 4.13 shows a successful detonation propagation of a 200 μm-thick PETN film. As previously mentioned the shock front forms a circular shape. Due to the detonation of the initial film seizing at the gap, the the distance between the reaction products and the shock front increases. As the second film is initiated the reaction products start to catch up to the shock front. This is because the shock to detonation transition is not instantaneous and takes a finite amount of time for reaction to build up to detonation.

The normal velocity plot shown, in Fig. 4.14, is for a 200 μm-thick film that successfully propagated across a 25 μm gap. It shows the decrease in the velocity of the shock front as the shape becomes circular. The shock front starts to speed up as the second film is initiated. The point where the shock front starts to speed up is at approximately 900 μm from the edge of the first film. The width of the gap is subtracted from this distance to estimate the distance to its steady-state wave shape. The distance to steady-state wave shape of this test was approximately 875 μm.

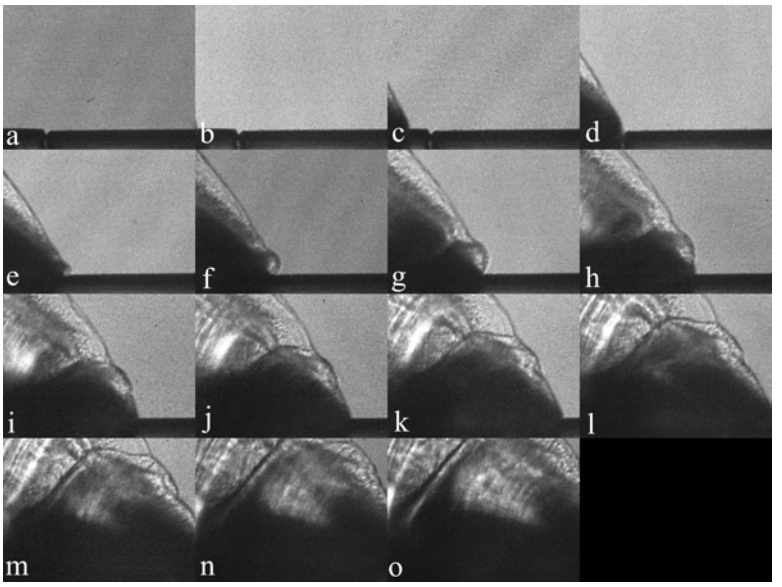

Figure 4.13: Focused shadowgraph images from Test 27 arranged from left to right then down. Test 27 is a gap test of a 200 μm-thick unconfined PETN film that successfully initiated the second film across a 25 μm gap.

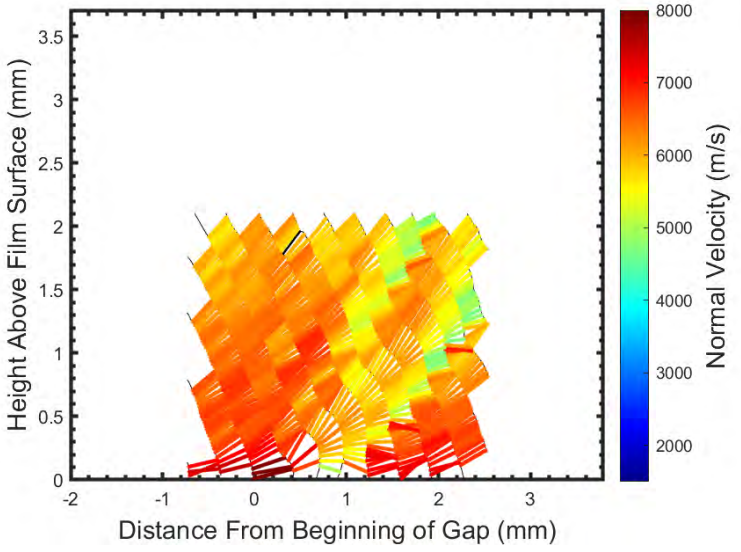

Figure 4.14: Normal velocity plot of Test 27. The tracked shock fronts from Test 27 were plotted as thin black lines. The black vectors represent vectors that did not meet the desired shock front matching uncertainty criteria.

The 400 μm-thick PETN films successfully propagated across larger gaps as shown in Fig. 4.15. The maximum run distance for a 400 μm-thick film is

greater than the maximum run distance for a 200 μm-thick film. This is because the run distance is limited by attenuation of the input shock wave at the edges by rarefactions [1]. Since the width of the films is significantly longer than the thickness, the thickness is the limiting factor for maximum run distance. In thicker films the rarefactions travel further before attenuating the peak pressure. The distance to its steady-state shock wave shape in the film shown, in Fig. 4.16, is approximately 1700 μm after accounting for the gap width. The distance to steady-state wave shape of this film is nearly double the distance to steady-state wave shape of the 200 μm-thick film discussed earlier.

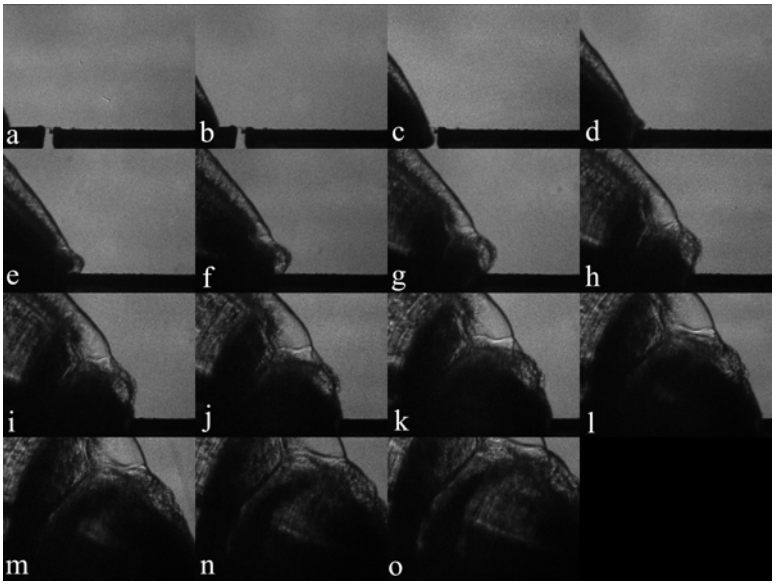

Figure 4.15: Schlieren images from Test 53 arranged from left to right then down. Test 53 is a gap test of a 400 μm-thick unconfined PETN film that successfully initiated the second film across a 220 μm gap.

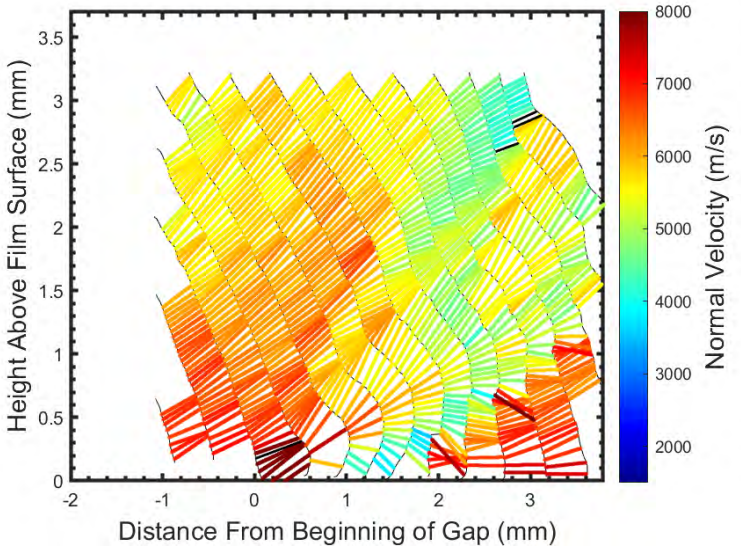

Figure 4.16: Normal velocity plot of Test 53. The tracked shock fronts from Test 53 were plotted as thin black lines. The black vectors represent vectors that did not meet the desired shock front matching uncertainty criteria.

4.2.3 Failed Initiation

The 70 μm-thick aluminum confined films were very close to the critical thickness of aluminum confined PETN of this deposition configuration (55 μm), and thus were not able to propagate across a gap that was separated only by the surface roughness.

In Fig. 4.17 the upper portion of the shock front looks rough, this portion of the shock front had not reached steady-state yet as is evident by Fig. 4.18 since the pre-gap shock front velocity drops significantly as the height above the film surface increases. For comparison purposes the velocity is steady until about 1.5 mm above the film surface at the vertical plane representing the beginning of the gap (0 mm from the beginning of the gap).

From the normal velocity plot in Fig. 4.18 it can be seen that the velocity slows down significantly after a detonation failure across the gap. The deceleration in shock velocity appears to propagate from the lower part of the shock front up.

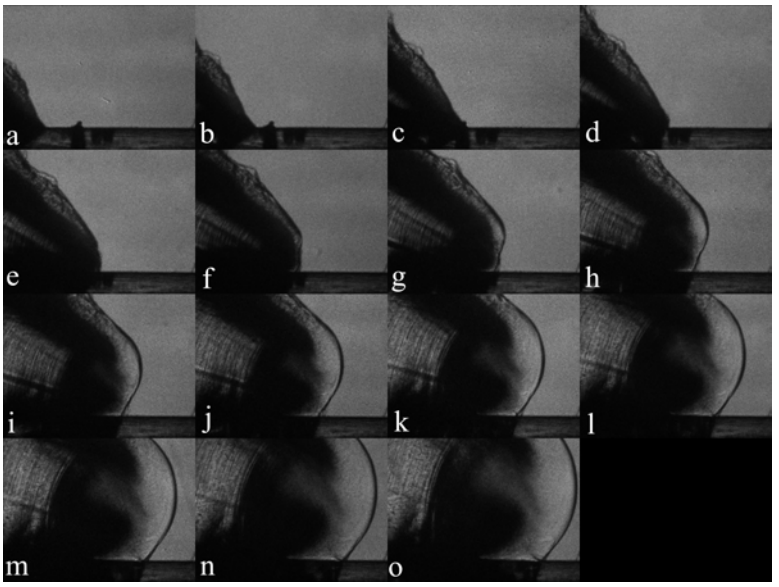

Figure 4.17: Schlieren images from Test 4 arranged from left to right then down. Test 4 is a gap test of a 70 μm-thick aluminum confined PETN film deposited on bare aluminum that failed to initiated the second film across a gap separated by the surface roughness.

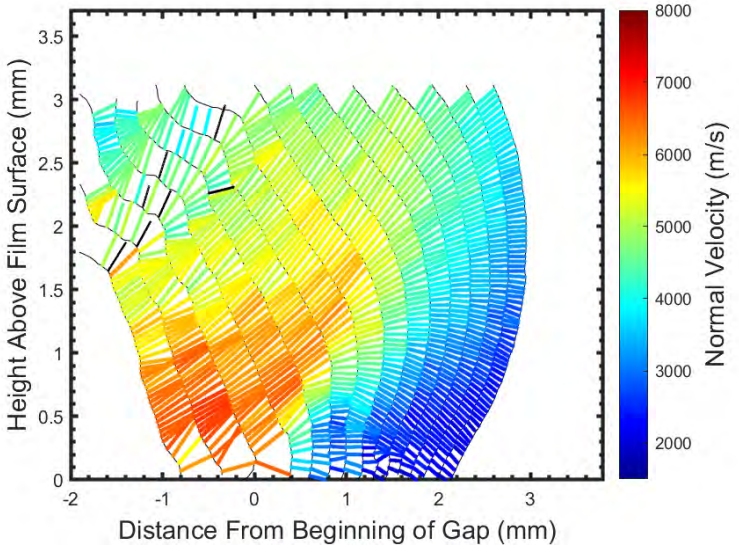

Figure 4.18: Normal velocity plot of Test 4. The tracked shock fronts from Test 4 were plotted as thin black lines. The black vectors represent vectors that did not meet the desired shock front matching uncertainty criteria.

The vertical alignment of the 70 μm-thick PETN film deposited on oxidized aluminum was slightly off between the two films as shown in Fig. 4.19.

The film failed to propagate across a gap separated only by the films surface roughness. The film reached steady detonation prior to reaching the gap and displayed no Mach stem like structures. Downstream of the gap multiple Mach stems appear ahead of the main shock front. The cause of the Mach stems may be from a shock reflection on the aluminum surface since the films were not perfectly aligned. Fig. 4.20 shows that the velocity of the shock front takes significantly longer to slow down. This is likely because the shock tracking algorithm extracted the front of the Mach stems which seem to decay at a slower rate than the main shock front, as evidenced by the increasing separation between the main shock front and the Mach stems in Fig. 4.19.

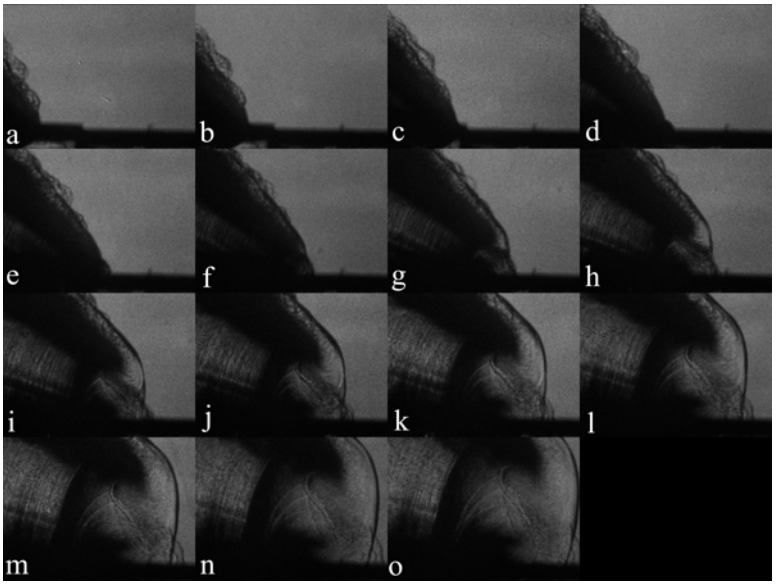

Figure 4.19: Schlieren images from Test 3 arranged from left to right then down. Test 3 is a gap test of a 70 μm-thick aluminum confined PETN film that failed to initiated the second film across a gap separated by the surface roughness.

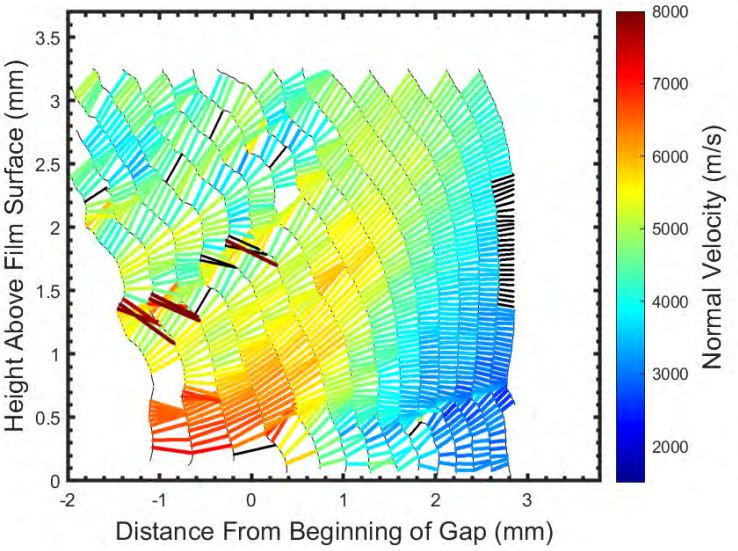

Figure 4.20: Normal velocity plot of Test 3. The tracked shock fronts from Test 3 were plotted as thin black lines. The black vectors represent vectors that did not meet the desired shock front matching uncertainty criteria.

Fig. 4.21 displays the image set for a 200 μm-thick PETN film that failed to propagate across a 93 μm gap. Previously, in the continuous film test section it was speculated that the 70 μm-thick films took longer to reach steady-state than the 200 μm-thick films. This was unconfirmed since the horizontal alignment was not recorded. However all the gap tests use a 1 cm-long substrate for the initial film as shown in Fig. 2.2. Fig. 4.22 shows that the 200 μm-thick film's air shock reached steady-state before crossing the gap, since the velocity of the pre-gap shock front is nearly uniform. With this in mind, it can now be conclusively proven that the 200 μm-thick PETN film reaches steady-state before the 70 μm-thick aluminum confined PETN films.

The height of the steady-state shock front above the film surface for the 70 μm-thick aluminum confined PETN films deposited on bare and oxidized aluminum were 1.5 mm and 1.1 mm, respectively. The steady-state height of the shock front for the 200 μm thick PETN film is approximately 2.1 mm above the height of the film. The height of the steady-state shock front may be higher, but the measurement was limited due to the small field of view used for this test. From this information it is concluded that the films deposited on bare aluminum take less time to reach steady-state than the films deposited on oxidized aluminum.

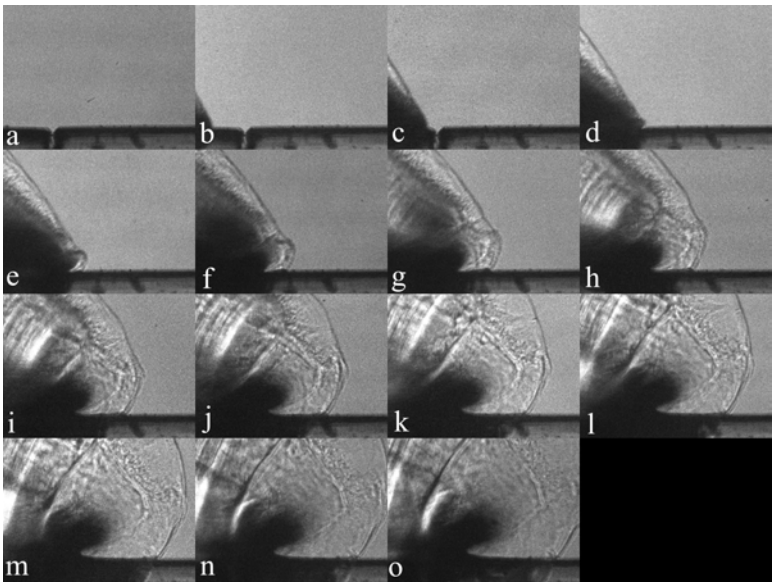

Figure 4.21: Focused shadowgraph images from Test 34 arranged from left to right then down. Test 34 is a gap test of a 200 μm-thick unconfined PETN film that failed to initiated the second film across a $\sim$93 μm gap.

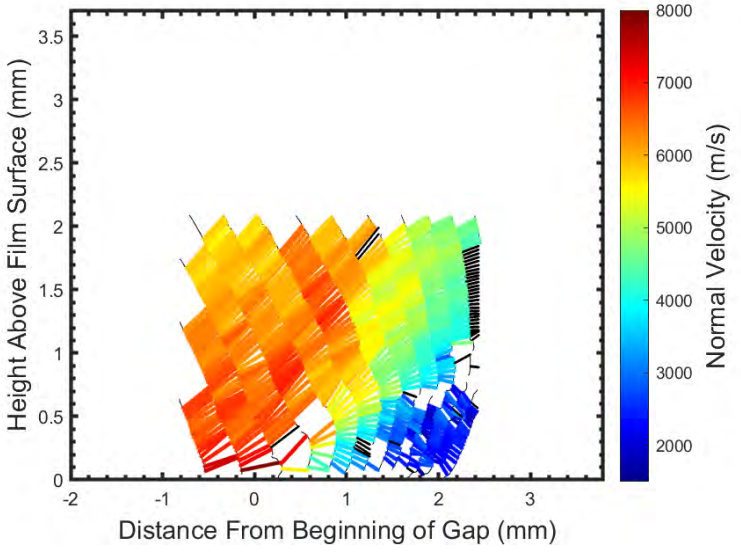

Figure 4.22: Normal velocity plot of Test 34. The tracked shock fronts from Test 34 were plotted as thin black lines. The black vectors represent vectors that did not meet the desired shock front matching uncertainty criteria.

The images of the 400 μm-thick film failing to propagate across a 200 μm gap shown, in Fig. 4.23, exhibit a slightly different post-gap shock front shape.

This shape changes from the circular post-gap shock front shape because the film is thick enough to drive the shock wave in the horizontal direction faster than the vertical direction. Fig. 4.24 is evidence of this, since it can clearly be seen that the shock front travels significantly further before decay than the shock front generated by thinner films. It can also be seen from Fig. 4.24 that the post-gap shock front is initially traveling at a higher velocity in the lower portion then decays faster than the upper portion of the shock front.

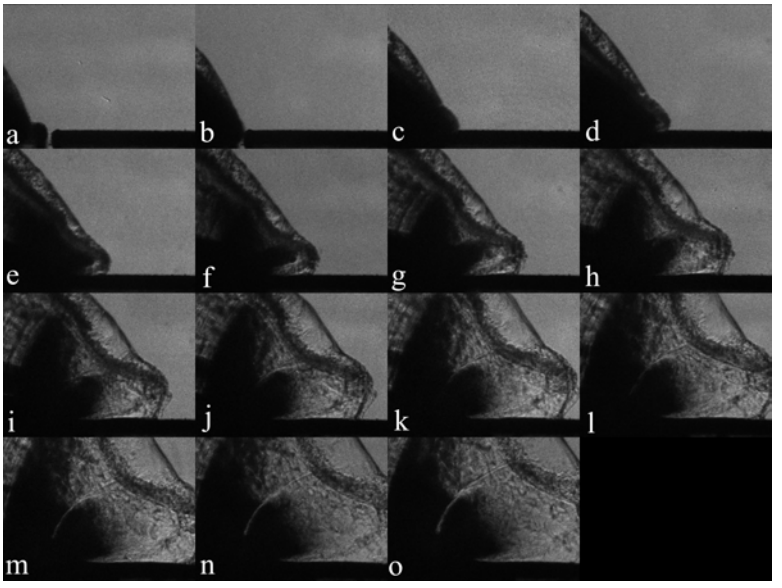

Figure 4.23: Schlieren images from Test 52 arranged from left to right then down. Test 52 is a gap test of a 400 μm-thick unconfined PETN film that failed to initiate the second film across a 200 μm gap.

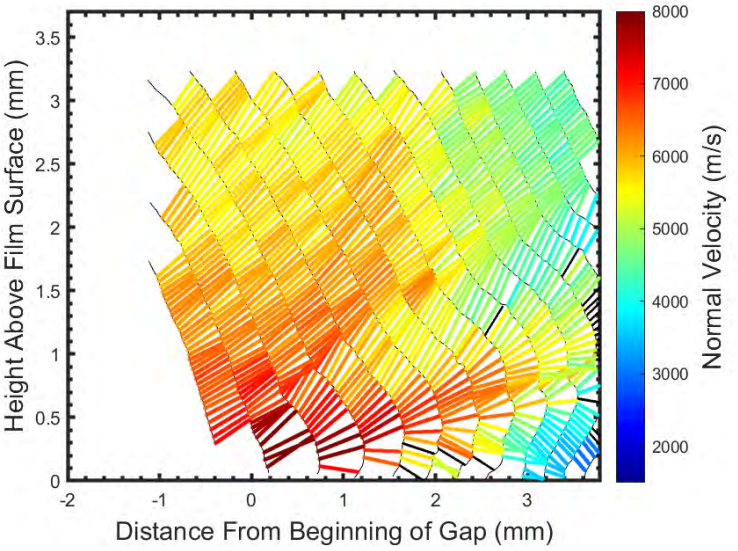

Figure 4.24: Normal velocity plot of Test 52. The tracked shock fronts from Test 52 were plotted as thin black lines. The black vectors represent vectors that did not meet the desired shock front matching uncertainty criteria.

4.3 Infinite Gap Test

The infinite gap test allows for the visualization of the shock front velocity decay as it propagates into free air. The axis limits for the infinite gap test are adjusted slightly from the limits used on the other gap tests. This was to account for the fact that in the infinite gap tests the end of the film was placed in roughly the center of the horizontal field of view. Although the axis limits of the infinite gap test are different than the gap test, the spatial scale remains the same for direct comparison to the gap tests.

Fig. 4.25 shows the images of an infinite gap test of a 70 μm-thick aluminum confined PETN film deposited on bare aluminum. The upper portion appears to be traveling faster than the lower portion as it starts to catch up in later time frames. As the shock front propagates into free air, the velocity of the shock front increases at the end of the film, as can be seen in Fig. 4.26. The acceleration doesn't last long and starts to decelerate shortly after. Fig. 4.26 shows that the upper is in fact traveling faster than the lower portion in late time frames.

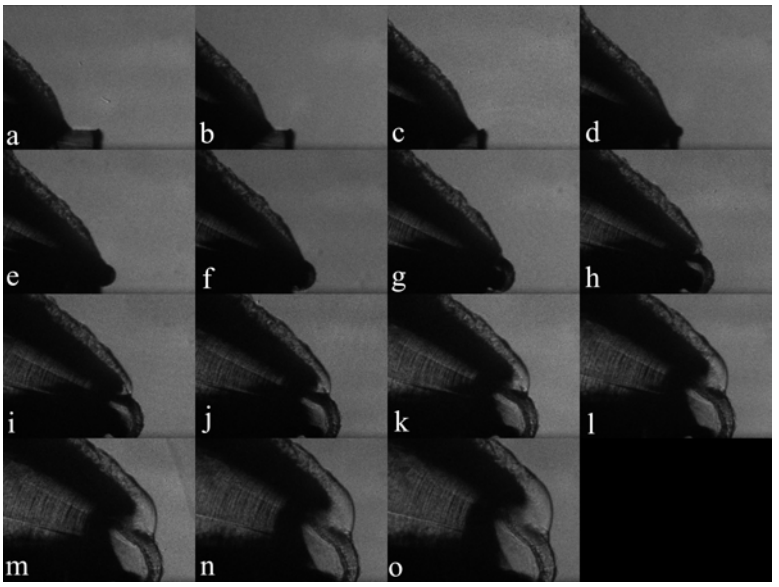

Figure 4.25: Schlieren images from Test 14 arranged from left to right then down. Test 14 is a infinite gap test of a 70 μm-thick aluminum confined PETN film deposited on bare aluminum.

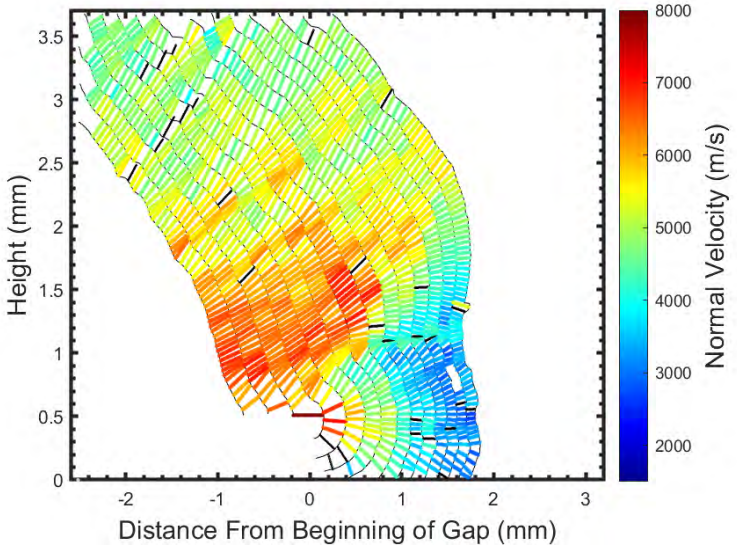

Figure 4.26: Normal velocity plot of Test 14. The tracked shock fronts from Test 14 were plotted as thin black lines. The black vectors represent vectors that did not meet the desired shock front matching uncertainty criteria.

The pre-gap shock front produced by the 70 μm-thick aluminum confined PETN film deposited on oxidized aluminum shown, in Fig. 4.27, is much

smoother than the pre-gap shock front produce by the 70 μm-thick aluminum confined PETN film deposited on oxidized aluminum shown in Fig. 4.25. It also appears to be much straighter.

The steady-state velocity of the 70 μm-thick aluminum confined PETN film deposited on bare aluminum is significantly higher as shown in Table 2.5. However, the difference in the velocity of the post gap shock front of the film deposited on oxidized aluminum is not significantly slower than the film deposited on bare aluminum. The velocities of the post gap shock front of the two separate films are surprisingly similar with only a small difference in velocity.

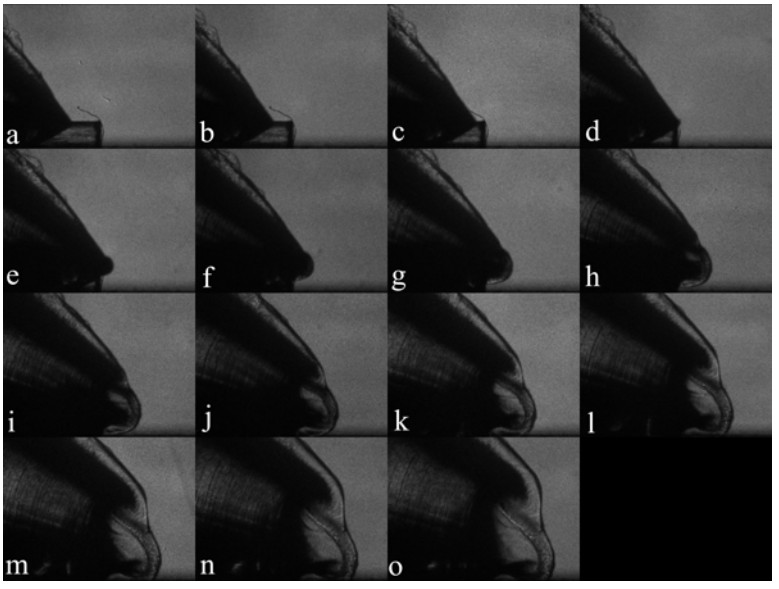

Figure 4.27: Schlieren images from Test 12 arranged from left to right then down. Test 12 is a infinite gap test of a 70 μm-thick aluminum confined PETN film deposited on oxidized aluminum

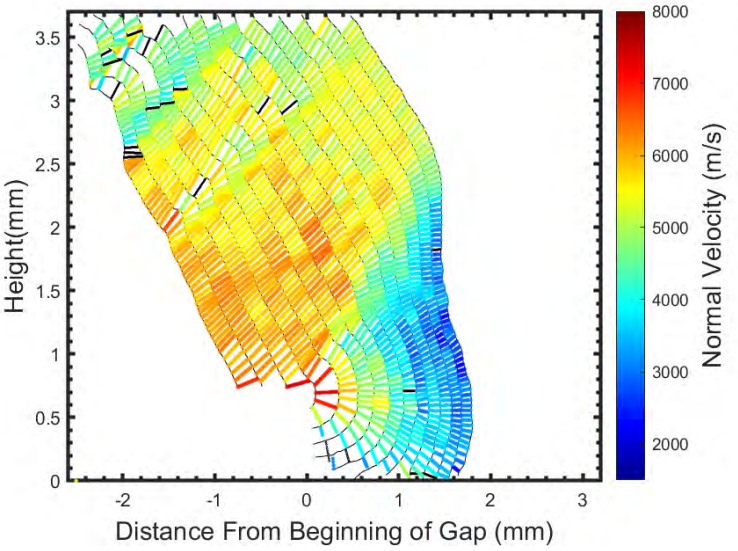

Figure 4.28: Normal velocity plot of Test 12. The tracked shock fronts from Test 12 were plotted as thin black lines. The black vectors represent vectors that did not meet the desired shock front matching uncertainty criteria.

The infinite gap test for a 200 μm-thick film is shown in Fig. 4.29. The shock front looks significantly different than the 70 μm-thick films shown in Fig. 4.25 and Fig. 4.27. It appears that the 200 μm-thick film drives the shock front in the horizontal direction more than the 70 μm-thick films.

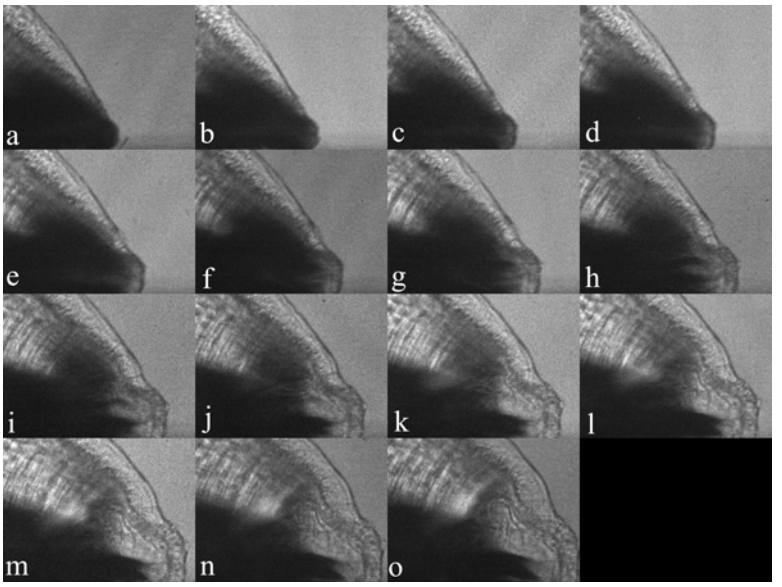

Figure 4.29: Focused shadowgraph images from Test 44 arranged from left to right then down. Test 44 is a infinite gap test of a 200 μm-thick unconfined PETN film.

The normal velocity plot of a 200 μm-thick infinite gap test is shown in Fig. 4.30. The velocity at the film height remains high for a substantially longer distance than the 70 μm-thick aluminum confined films. However, after approximately 1 mm from the beginning of the gap, the velocity drops rapidly. The velocity of the shock front at the film height is calculated by individually extracting the velocity values along the points shown in the box of Fig. 4.31. The values are plotted in Fig. 4.32. There is some scatter likely due to the rough shape of the shock front.

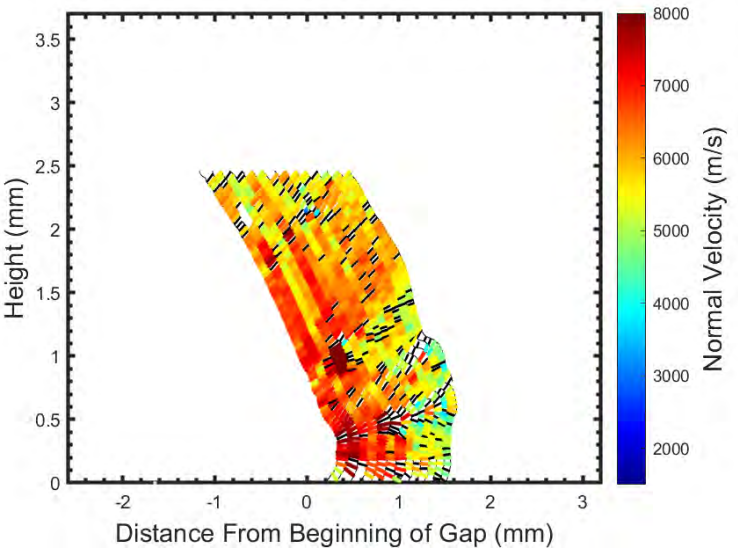

Figure 4.30: Normal velocity plot of Test 44. The tracked shock fronts from Test 44 were plotted as thin black lines. The black vectors represent vectors that did not meet the desired shock front matching uncertainty criteria.

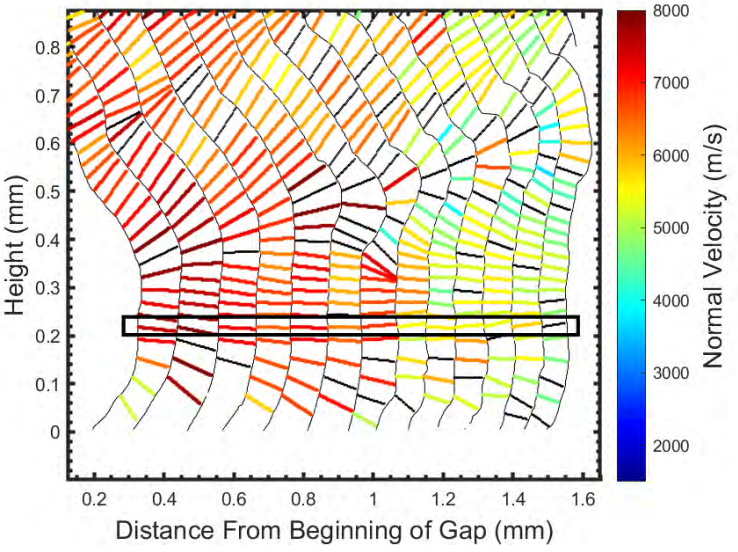

Figure 4.31: Close up section of Fig. 4.30. The vectors inside the black box are used for the velocity determination in Fig. 4.32

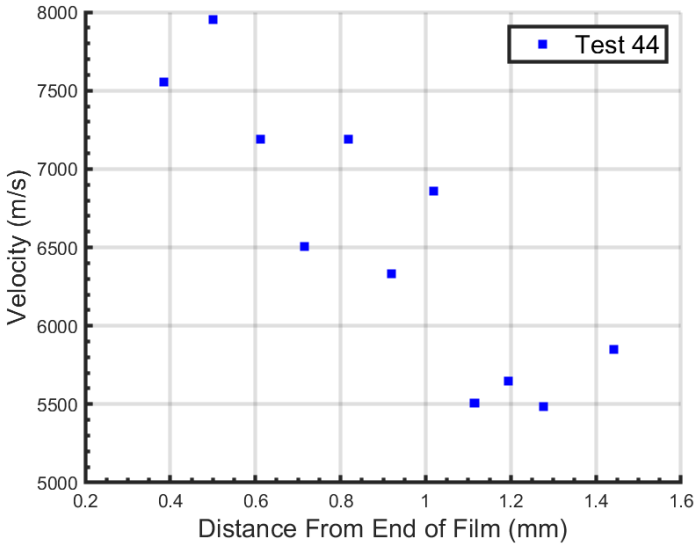

Figure 4.32: Velocity of the shock front at the film height determined from the vectors located in the black box of Fig. 4.31

CHAPTER 5

COMPUTATIONAL RESULTS

The 200 μm-thick unconfined PETN films were modeled with CTH and computer generated schlieren (CGS) images were created from the density output. After minor adjustments to the model, the films were able to initiate at a film thickness of 200 μm. The critical gap width was explored, and was found to be 125 μm. Table 5.1 outlines the results for detonation propagation of the films simulated.

Table 5.1: CTH test failure table.

Test #	Film Thickness (μm)	Gap Width (μm)	Detonation Propagation
CTH 1	200	50	Yes
CTH 2	200	100	Yes
CTH 3	200	125	Yes
CTH 4	200	150	No
CTH 5	200	200	No
CTH 6	200	inf	N/A

5.1 Continuous Film

The continuous film test was conducted by using early time frames of Test CTH 2. The shock wave reached its steady-state shape well ahead of the gap and thus Test CTH 2 provided sufficient steady-state pre-gap frames. Therefore a discrete continuous film test was not necessary. The uniformity of the pre-gap velocity results of Test CTH 2 can be seen in the velocity plot in Fig. 5.1. The continuous film velocity plot in Fig. 5.1 was of a smaller scale and the x and y axis were both shrunk by a factor of 2 to keep the same aspect ratio as the other CTH plots. The detonation velocity taken along the top edge of the PETN film in the horizontal direction is shown in Table 5.2. The velocity is slightly lower than

the velocity from the experimental shock front measurement and fiber probe lid measurement.

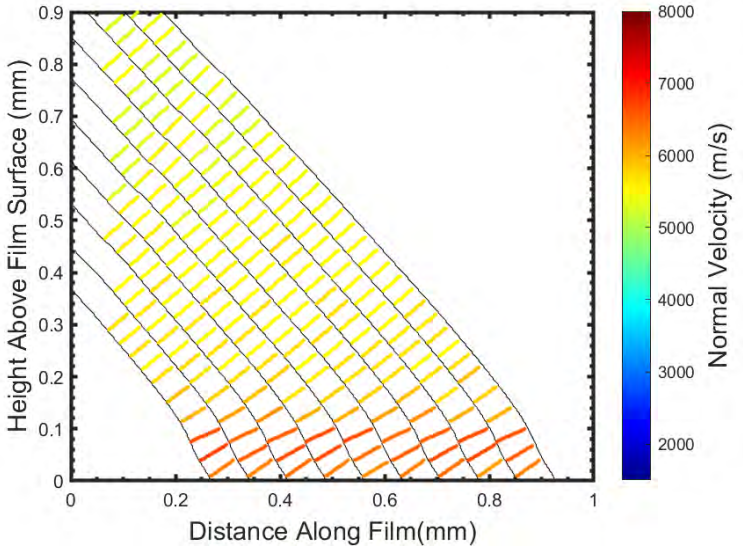

Figure 5.1: Continuous velocity measurement. Data was extracted from the steady-state section of Test CTH 2. The inter-frame time between shock fronts is 10 ns.

Table 5.2: Detonation velocity comparison table.

Test #	Film Thickness (μm)	Detonation Velocity (m/s)	Substrate Material	Measurement
1	70	7450 ± 116	Oxidized Aluminum	Shock Front
2	70	7910 ± 53	Bare Aluminum	Shock Front
21	200	7651 ± 197	Polycarbonate	Shock Front
22	200	7513 ± 135	Polycarbonate	Shock Front
Fiber Probe 1	200	7536 ± 31	Polycarbonate	Fiber Probe Lid
Fiber Probe 2	200	7391 ± 251	Polycarbonate	Fiber Probe Lid
CTH 2	200	7319 ± 88	PMMA	Shock Front

5.2 Gap Tests

Neither the PETN films nor the PMMA substrates are visible in the CGS images. This is a result of a derivative being performed over density. Since the density of the PETN is constant, only the vertical edges of the films are highlighted. Fig. 5.2 shows a density image from Test CTH 1 for visualization of where the PETN films lie in the CGS images in this section.

Figure 5.2: Density image for visualization of PETN location.

5.2.1 Successful Initiation

The CGS images look very similar to the experimental images, except for a less pronounced circular air shock. In the experiments the outward protrusion in the shock front after the detonation passes the gap is now in the shape of a notch. A comparison between the outward protrusion and the notch is shown in Fig. 5.3. In the experimental images the air shock produced by the initial film travels further than the slower moving reaction in the second film. This causes the air shock from the initial film to form a circular protrusion over the second film. The second film has a long run distance and by the time detonation occurs, the air shock from the initial film has traveled further. The detonation of the second film is much faster than the decaying air shock from the first film. Thus the air shock produced by the detonation of the second film eventually overtakes the air shock from the first film and the film returns to its steady-state wave shape.

In the CTH tests, the second film initiates almost immediately without allowing the air shock from the first film to surpass it. The protrusion does not

have a chance to form. Therefore the run distance to detonation is significantly shorter in the CTH tests than the experimental tests.

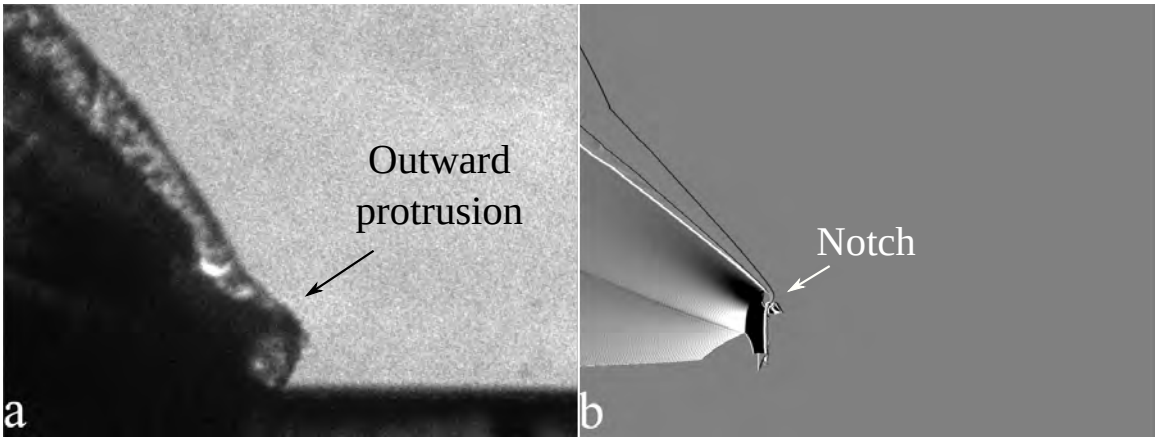

Figure 5.3: Comparison between a schlieren image from a successful propagation test (Test 46) and a CGS image from a successful propagation test (CTH 1). a) The schlieren image shows the air shock from the initial film forming an outward protrusion over the second film. b) The CGS image shows the second film initiating before the air shock from the initial film has a chance to form a protrusion. This creates a notch in between the two air shocks.

In Fig. 5.4c a protrusion starts to form since the gap width of 100 μm is larger than the gap width of 50 μm shown in Fig. 5.5. The extra width of the gap allows for the attenuation in pressure of the incident air shock. This lower incident pressure requires a longer run distance to initiate the PETN. The run distance is still relatively short and the protrusion is overtaken by the detonation of the second film as can be seen in Fig. 5.4d.

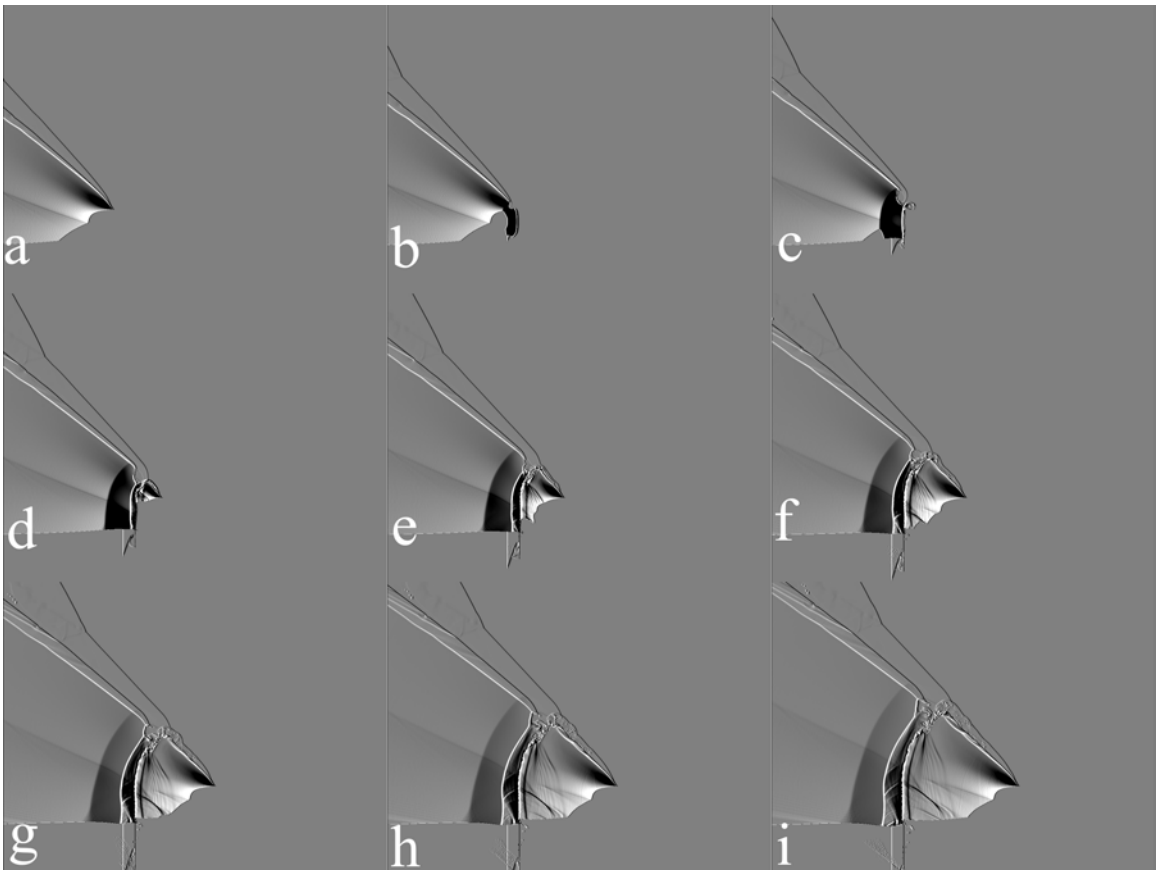

Figure 5.4: Computer generated schlieren images from a a 100 μm-gap-width gap test (Test CTH 2). The inter-frame time between images is 20 ns.

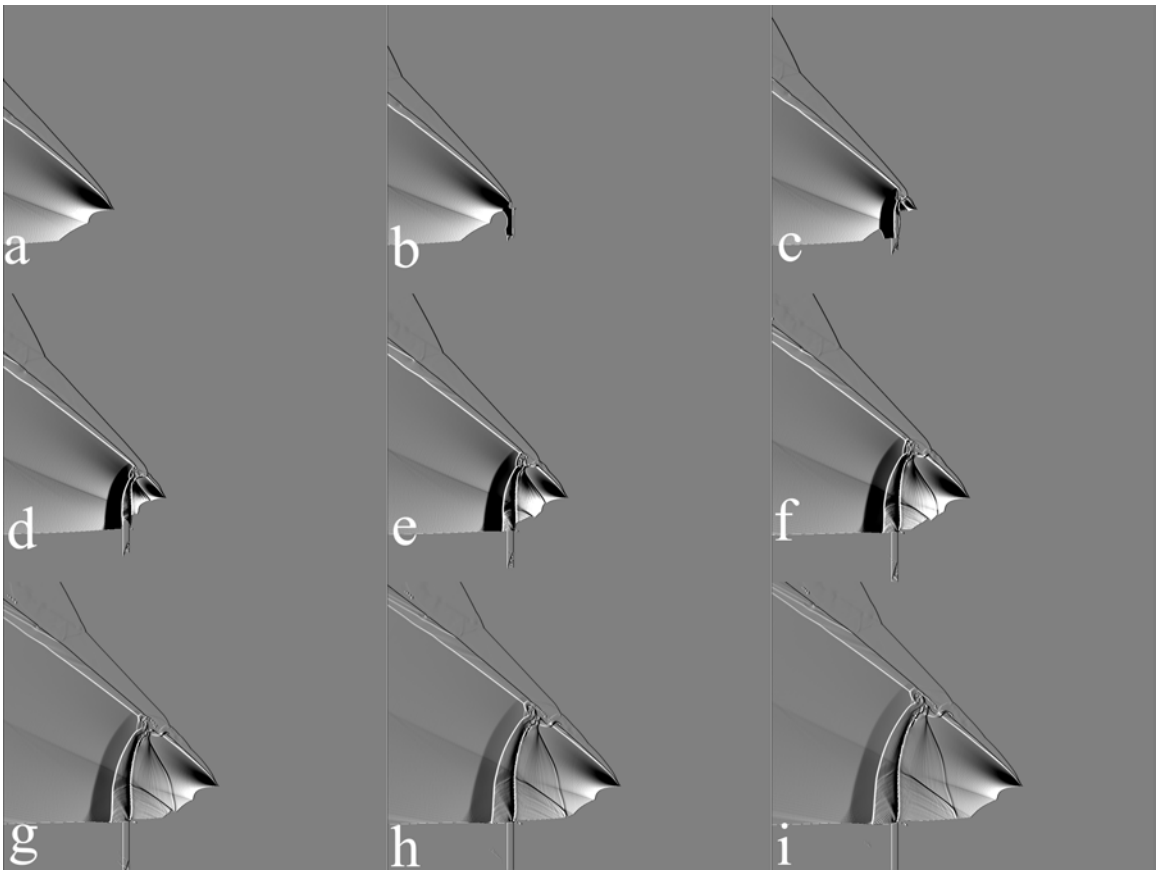

Figure 5.5: Computer generated schlieren image from a a 50 μm-gap gap test (Test CTH 1). The inter-frame time between images is 20 ns.

The initiation of the second films does occur sooner in the CTH simulations than in the experimental tests. This can be observed in Figs. 5.6 and 5.7. The distance to a steady-state shock shape in a 50 μm-gap-width gap test shown in Fig. 5.6 is approximately 70 μm after accounting for the gap width. The distance to a steady-state shock shape in the 100 μm-gap-width gap test (CTH 2) is approximately 200 μm. Both of these distances obtained from the CTH simulations are significantly shorter than the 875 μm distance to a steady-state shock shape found from a 200 μm-thick PETN film with a gap width of 25 μm (Test 26). The CGS images have an upper region of the shock front that is at a higher velocity than the rest of the shock front as seen in Fig. 5.6. This is due to the effects of the initiation structure.

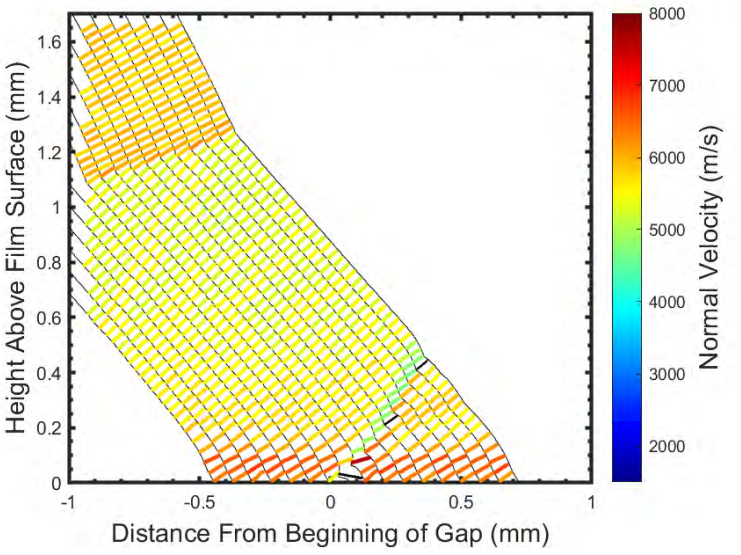

Figure 5.6: Normal velocity plot of Test CTH 1. The tracked shock fronts from Test CTH 1 were plotted as thin black lines. The black vectors represent vectors that did not meet the desired shock front matching uncertainty criteria. The inter-frame time between shock fronts is 10 ns.

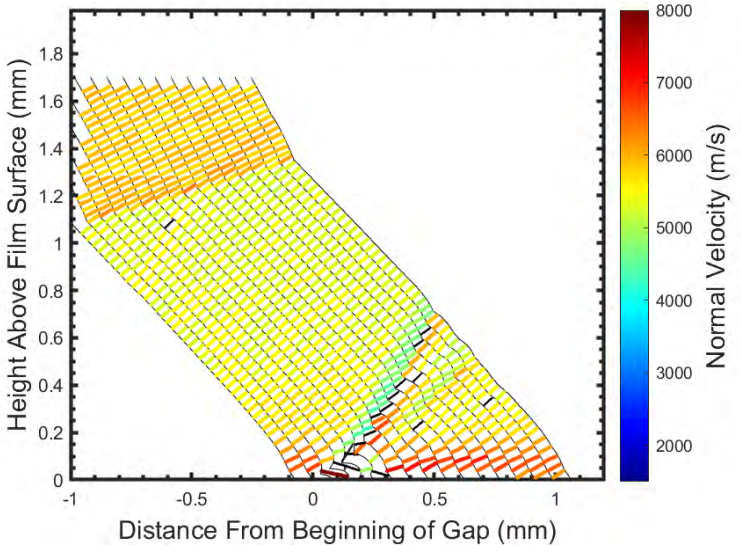

Figure 5.7: Normal velocity plot of Test CTH 2. The tracked shock fronts from Test CTH 2 were plotted as thin black lines. The black vectors represent vectors that did not meet the desired shock front matching uncertainty criteria. The inter-frame time between shock fronts is 10 ns.

5.2.2 Failed Initiation

The 200 μm-gap-width (CTH 5) resulted in a failure to initiate the second film. The shock front shown in Fig. 5.8 displays a significant separation between the lower and upper sections, which results in a notch between the two sections. As the shock traveled further, the two sections coalesce into one. The lower and upper sections of the shock front show a small discontinuity in the experimental images, however, it is to a much lesser extent.

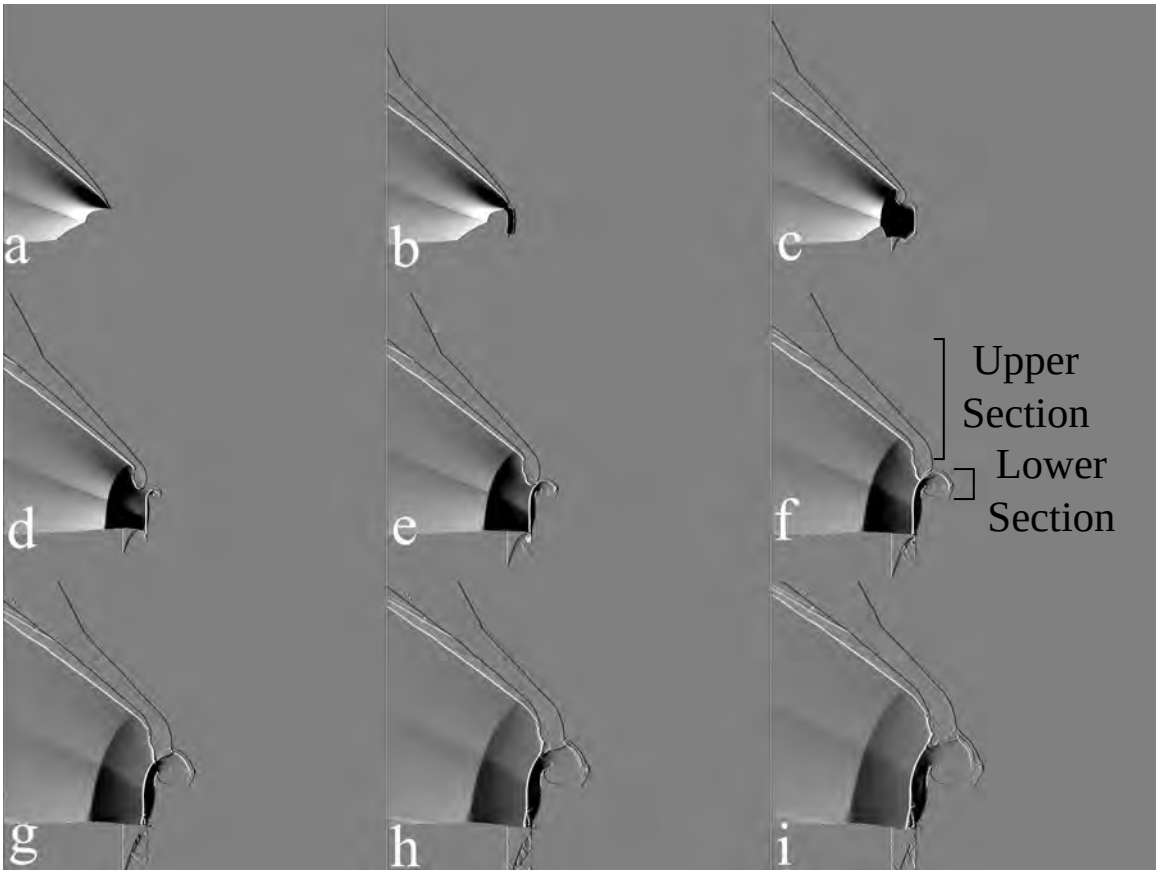

Figure 5.8: Computer generated schlieren image from a a 200 μm-gap-width gap test. The inter-frame time between images is 20 ns.

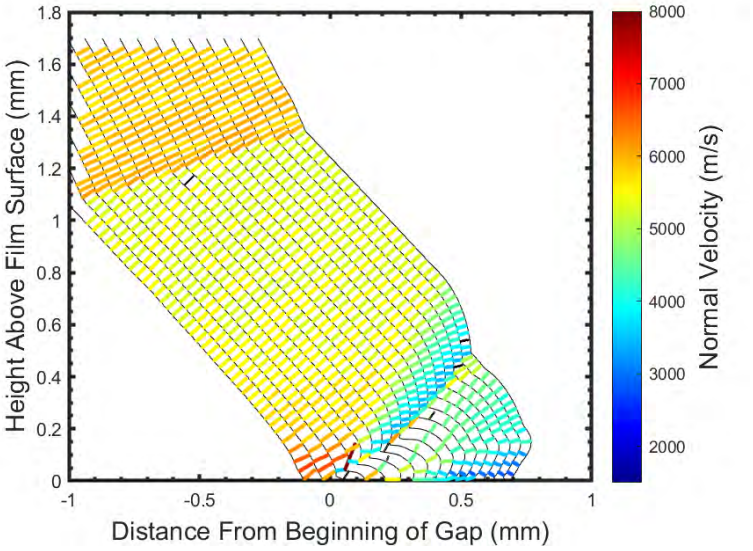

Figure 5.9: Normal velocity plot of Test CTH 5. The tracked shock fronts from Test CTH 5 were plotted as thin black lines. The black vectors represent vectors that did not meet the desired shock front matching uncertainty criteria. The inter-frame time between shock fronts is 10 ns.

5.2.3 Infinite Gap

The infinite gap test shown in Fig. 5.10 displays significant separation between the lower and upper portions of the shock front as has been seen in all the CGS images. The lower portion of the shock front seems to be traveling at a significantly faster velocity than the lower portion of the shock front in the experimental test. In the velocity plot shown in Fig. 5.11, the shock front seems to travel at a similar rate as the experimental images. However, there is a significant drop in velocity slightly above and below the film surface, that is not seen in the experimental images.

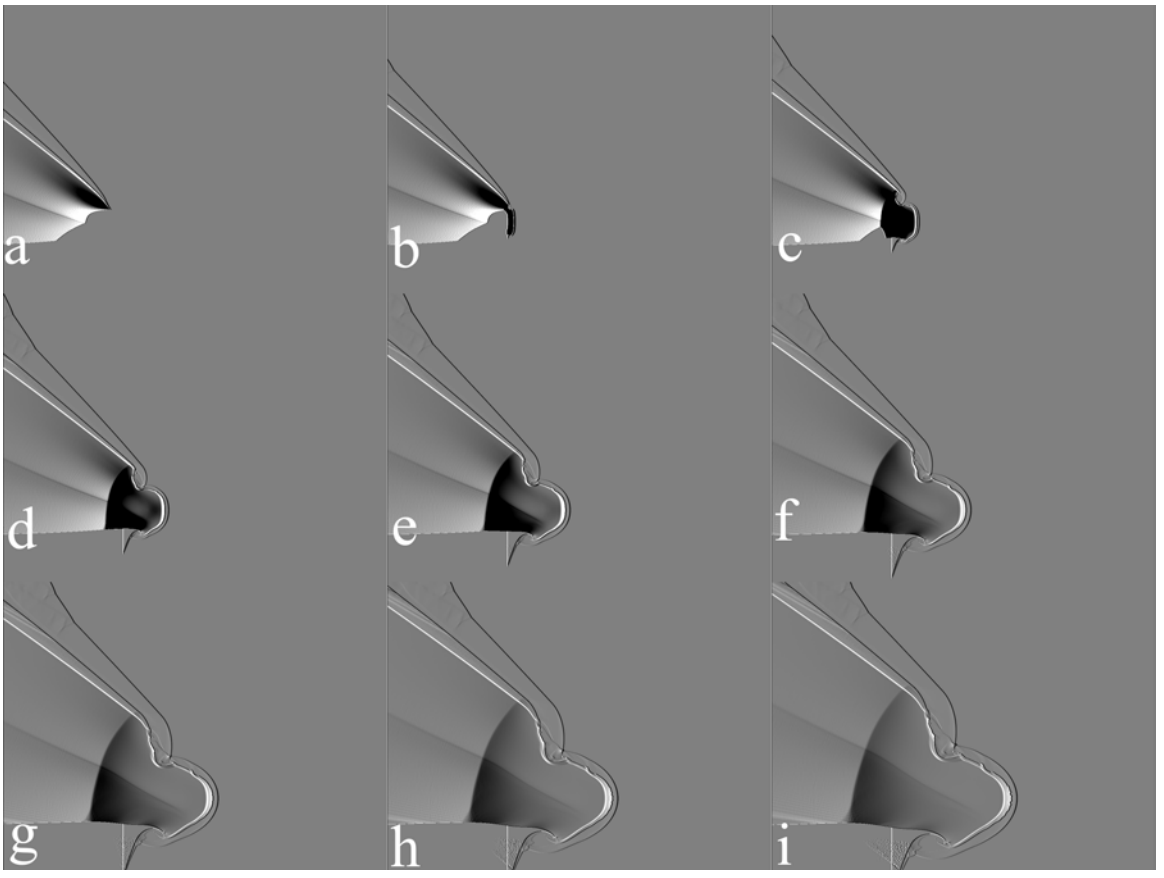

Figure 5.10: Computer generated schlieren images from an infinite gap test (Test CTH 6). The inter-frame time between images is 20 ns.

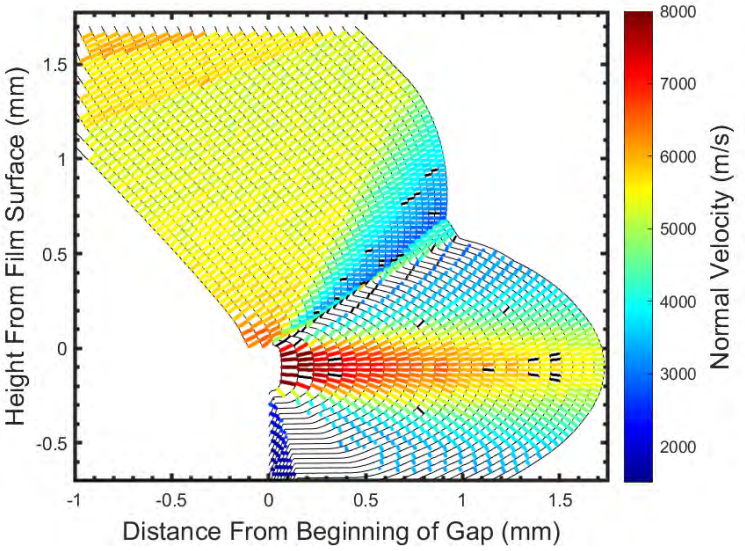

Figure 5.11: Normal velocity plot of Test CTH 6. The tracked shock fronts from Test CTH 6 were plotted as thin black lines. The black vectors represent vectors that did not meet the desired shock front matching uncertainty criteria. The inter-frame time between shock fronts is 10 ns.

The velocity values enclosed in the black box of Fig. 5.12 were extracted for comparison with experiments. The location of the velocity values is based off of the center of each vector. These velocity values were compared in Fig. 5.13 to the velocity values taken using the same method from Test 44. The trend matches fairly well, with the computational data trend being slightly lower than the trend of the experimental data. This is expected since the 200 μm-thick CTH PETN films had a lower detonation velocity than the 200 μm-thick PETN films in the experiments.

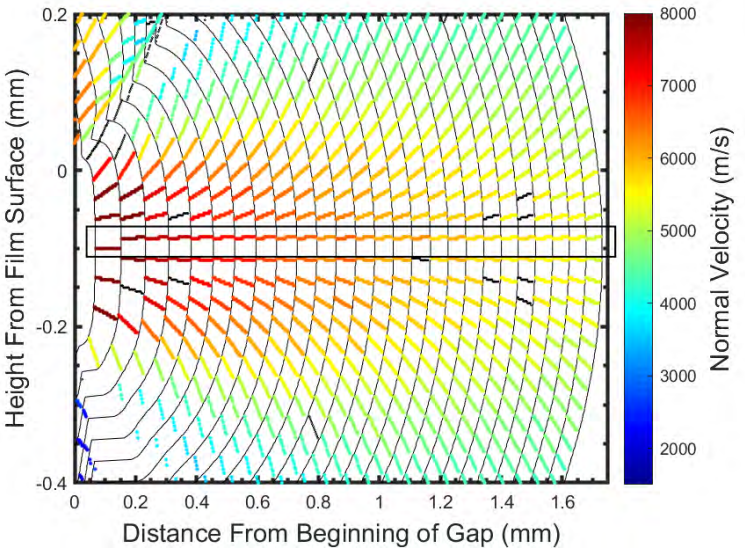

Figure 5.12: Close up section of Fig. 5.11. The vectors inside the black box are used for the velocity determination in Fig. 5.13

.

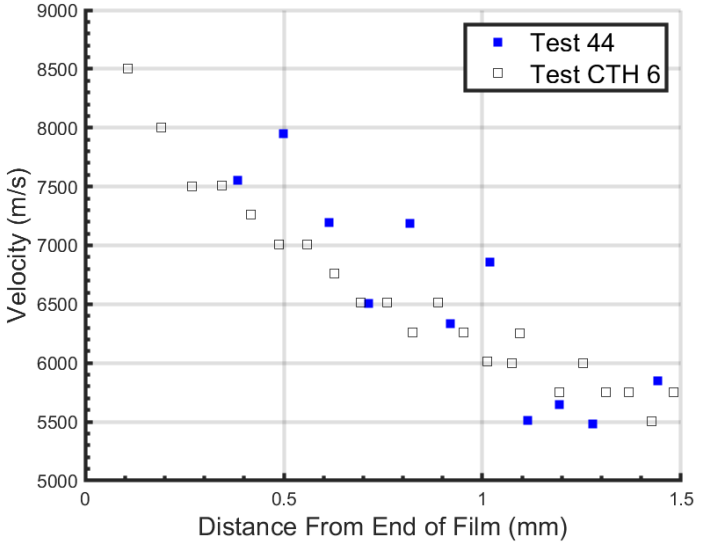

Figure 5.13: Comparison of velocity normal to the end of the film in Test 44 and Test CTH 6.

5.2.4 Distance to Steady-State Wave Shape

The distance to the steady-state wave shape discussed in Chapter 2 is explored further here. The detonation within the film can be seen in CGS images with a simple histogram shift. Figure 5.14 shows the evolution of the detonation as it catches up to the air shock to reach its steady-state wave shape. At time t=0 the film has already been initiated and the detonation is starting to propagate outward. 11 nanoseconds later (t=11) the detonation emerges from the film surface. The detonation is significantly behind the air shock. 7 nanoseconds after the detonation emerges from the film surface (t=18), the detonation catches up with the air shock from the initial film.

There was only a 18 nanosecond delay from the approximate initiation point to when the shock front reached its steady-state wave shape. However, in the experimental images the run distance is significantly longer, allowing the initial air shock to travel a significant amount of distance before the detonation catches up.

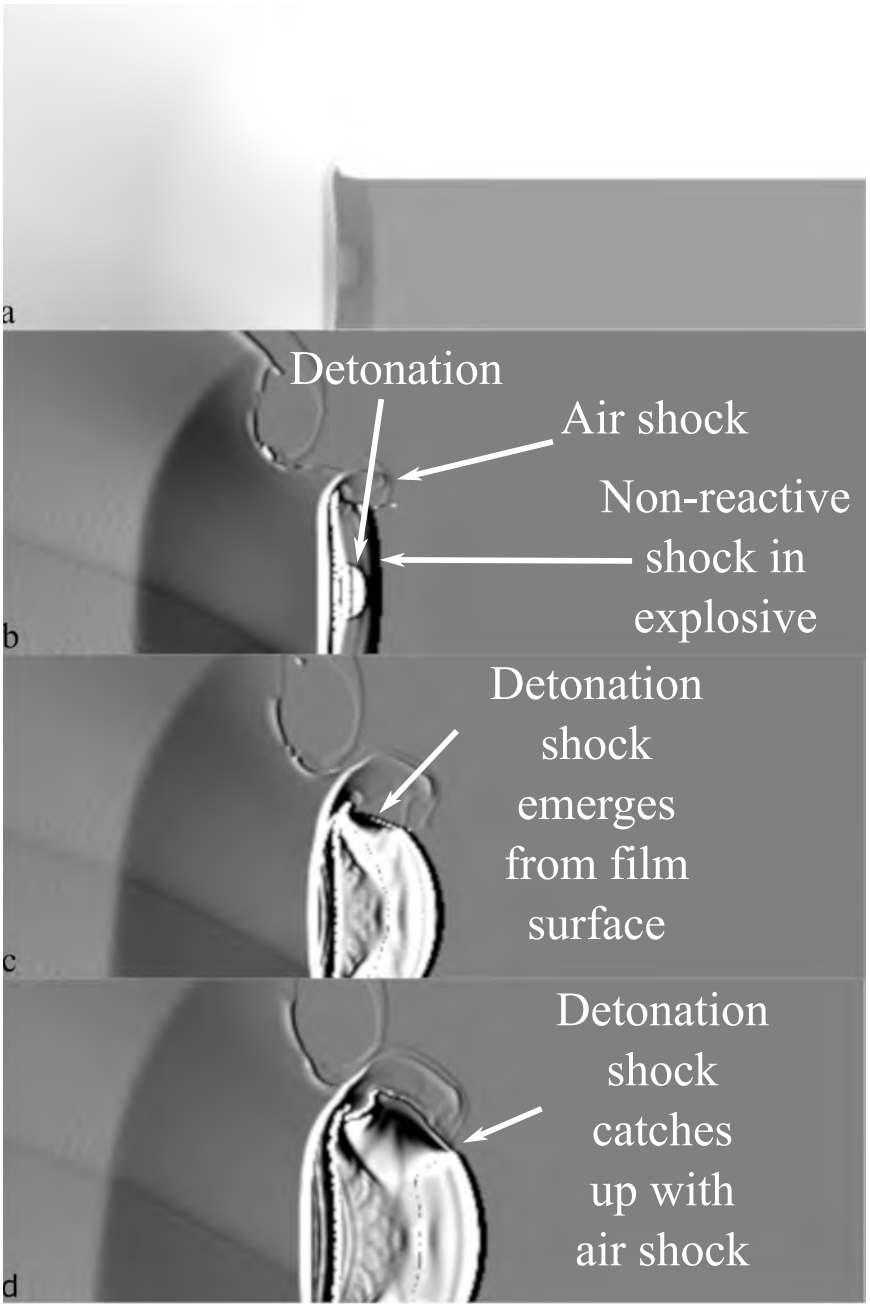

Figure 5.14: Evolution from the detonation formation within the explosive to the time it reaches its steady-state wave shape. The images were taken from Test CTH 3. a) Density image to visualize the location of the PETN film at t=0. b) The air shock from the initial film forms over the second film. The film is initiated and the detonation is making its way toward the edges of the film, t=0 ns. c) The detonation shock emerges from the edge of the film. The air shock is significantly ahead of the detonation, t=11 ns. d) The detonation catches up with the air shock. This is the point where the shock reaches its steady-state wave shape, t=18 ns.

CHAPTER 6

CONCLUSION

Experiments and computations were performed to visualize PETN films detonating across microcracks. The microcracks were found to have a significant effect on films that were close to their critical thickness. This was determined by the failure of detonation to propagate across abutment gaps in films close to their critical thickness. The cracks had a lesser effect on films well above their critical thickness as was evidenced by their relatively large critical gap widths. The unconfined films had a critical gap width that appears to scale with thickness. The 400 μm-thick PETN films had a critical gap width of 180 μm which is approximately double the 80 μm critical gap width belonging to the 200 μm-thick PETN films.

Refractive imaging was used to determine detonation propagation/failure across the gaps. In addition to this binary output, the detonation velocity as well as shock wave velocity were extracted using image processing methods. The image processing methods allowed for the extraction of the spatial location along the shock front. The knowledge of the spatial location along the shock front allows for the velocity to be calculated across the entire shock front. With the implementation of the normal velocity calculations the velocity was calculated at several discrete locations in the direction of flow. The normal velocity plots allowed for a quantitative determination of the steady-state regions of the shock front.

The refractive imaging along with the normal velocity plots revealed that the gaps cause a significant disruption in the shape of the wave. The gaps allow the air shock from the initial film to travel a significant distance before the detonation front catches up.

The shock front produced by the 70 μm-thick aluminum confined films started out with a very non-uniform shape. The non-uniformity was likely caused by porosity, that was able to have a significant effect due to the extremely thin thickness of the films. The non-uniformity in the shock front eventually evolved into a uniform shape as the detonation traveled along the film. It was determined that the 70 μm-thick aluminum confined films take longer to reach their steady shape than the 200 μm-thick unconfined PETN films as determined by the height of the steady-state velocity at the end of the initial film.

The CTH simulations matched the experiments fairly well. The critical gap with for a 200 μm-thick PETN film in the simulations was found to be 125

μm, which was higher than the 80 μm-gap-width found in the experiments at the same film thickness. Although the critical gap width was higher in the simulations, the simulation provided reasonable results with only minor alterations to the solid phase equation of state and burn rate model. The computer generated schlieren (CGS) images allowed for visualization of the detonation within the explosive, which was not possible with the use of refractive imaging in the experiments. This new capability allowed for the the determination of the time it takes for the shock front to reach its steady-state wave shape after detonation. The distance to a steady-state wave shape in the simulations was significantly shorter than the experiments. Although the distance to a steady-state wave shape is shorter than the experiments, it is by no means instantaneous. In the simulations it took approximately 18 nanoseconds to reach the steady-state wave shape. As a result of the quicker initiation time in the simulations, the shock front did not form an outward protrusion in the successful detonation propagation gap tests. Instead a notch was formed between the air shock of the first film and the air shock of the second film.

The air shock infinite gap test simulation displayed a similar shape to the experiments. The velocity at the film height compared favorably between the simulation and the experiments. Surprisingly above and below the film height, the velocity of the air shock showed significant velocity attenuation, that was not present in the experiments.

Each PETN film used here was deposited on a polycarbonate substrate, some of which used a 1 μm-thick aluminum layer between the polycarbonate substrate and the PETN. The effect of the shock impedance of the substrate was not explored. The shock impedance of the one sided confinement used here could affect the detonation properties including the critical gap width.

6.1 Future Research

The microcracks were found to have a significant effect on the performance of the films. In use of explosive that may contain microcracks, the engineer should be wary of potential effects the microcracks can have beyond the detonation failure across gaps that was explored here. The work here explored single microcracks, however, in an explosive with several microcracks, the detonation time of arrival may be significantly delayed. This would occur since the build up to reaction that occurs after a crack, would happen several times, thus introducing latency.

It has been found here that as the detonation reaches a crack the air shock travels along the second film unsupported. As the air shock travels along the second film the detonation is building up and thus moving at a slower speed. In an explosive system, the unsupported air shock from the initial film may arrive at the intended acceptor explosive before the detonation front. Since the unsupported air shock is attenuating, the pressure of the air shock may not be enough to initiate the acceptor explosive. This could then cause the acceptor explosive to

become inert in the locations the shock passes through creating dead zones [74]. In the case where the stronger air shock produced by the detonation reaches the acceptor explosive after the unsupported air shock, the acceptor explosive would not be able to initiate until the shock from the supported detonation reaches the unsupported air shock from the initial film. If this distance is long enough, it could render the supported shock from the detonation too weak to initiate the the acceptor explosive.

REFERENCES

[1] Paul W. Cooper. *Explosives Engineering*. Wiley-VCH, 1996.

[2] Wildon Fickett and William C. Davis. *Detonation: Theory and Experiment*. Dover Publications, 2000.

[3] Herbert T. Knight and Douglas Venable. Apparatus for Precision Flash Radiograhpy of Shock and Detonation Waves in Gases. *Review of Scientific Instruments*, 29(2):92–98, 1958.

[4] John M. Densmore, Matthew M. Biss, Kevin L. McNesby, and Barrie E. Homan. High-Speed Digital Color Imaging Pyrometry. *Applied Optics*, 50(17):2659–2665, 2011.

[5] John M. McAfee, Blaine W. Asay, A. Wayne Campbell, and John B. Ramsay. Deflagration to Detonation in Granular HMX. Report No. LA-UR–91-2103, Los Alamos National Laboratory, 1991.

[6] Daniel H. Dolan. Foundations of VISAR Analysis. Report No. SAND2006-1950, Sandia National Laboratories, 2006.

[7] Kevin J. Fleming and Theresa A. Broyles. Shock Analysis Using the Multi Point Velocimeter (VISAR). Report No. SAND2003-3759, Sandia National Laboratories, 2003.

[8] L. M. Barker and R. E. Hollenbach. Laser Interferometer for Measuring High Velocities of any Reflecting Surface. *Journal of Applied Physics*, 43:4669–4675, 1972.

[9] O. T. Strand, D. R. Goosman, C. Martinez, and T. L. Whitworth. Compact System for High-Speed Velocimetry Using Heterodyne Techniques. *Review of Scientific Instruments*, 2006.

[10] V. Bouyer, M. Doucet, and L. Decaris. Experimental Measurements of the Detonation Wave Profile in a TATB Based Explosive. *EPJ Web of Conferences*, 10:00030, 2010.

[11] A. W. Campbell, M. E. Malin, T. J. Boyd Jr., and J. A. Hull. Precision Measurement of Detonation Velocities in Liquid and Solid Explosives. *The Review of Scientific Instruments*, 27(8):567–574, 1956.

[12] Wim Prinse, Rene van Esveld, Rene Oostdam, Murk van Rooijen, and Richard Bouma. Fibre-Optical Techniques for Measuring Various Properties of Shock Waves. *Proceedings of SPIE 3516, 23rd International Congress on High-Speed Photography and Photonics*, 1999.

[13] Jerry Benterou, Corey V. Bennett, Garrett Cole, D. E. Hare, Chadd May, Eric Udd, Stephen J. Mihailov, and Ping Lu. Embedded Fiber-Optic Bragg Grating (FBG) Detonation Velocity Sensor. *Proceedings of SPIE, Fiber Optic Sensors and Applications VI*, 7316:73160E, 2009.

[14] G. Rodriguez, R. L. Sandberg, Q. McCulloch, S. I. Jackson, S. W. Vincent, and E. Udd. Chirped Fiber Bragg Grating Detonation Velocity Sensing. *Review of Scientific Instruments*, 2013.

[15] Melvin A. Cook, Ray L. Doran, and Glen J. Morres. Measurement of Detonation Velocity by the Doppler Effect at Three-Centimeter Wavelength. *Journal of Applied Physics*, 26(4):426–428, 1954.

[16] A. W. Campbell and Ray Engelke. The Diameter Effect in High-Density Heterogeneous Explosives. In *Proceedings of the Sixth Symposium (International) on Detonation*, pages 642–651, Coronado, California, August 1976.

[17] Hartmut Badners and Carl-Otto Leiber. Method for the Determination of the Critical Diameter of High Velocity Detonation by Conical Geometry. *Propellants, Explosives, Pyrotechnics*, 17:77–81, 1992.

[18] B. M. Dobratz and P. C. Crawford. *LLNL Explosives Handbook - Properties of Chemical Explosives and Explosive Simulants*. 1985.

[19] Donna Price, A. R. Clairmont, and J. O. Erkman. The NOL Large Scale Gap Test . III. Compilation of Unclassified Data Suplementary Information for Interpretation of Results. Report No. NOLTR 74-40, Naval Ordnance Laboratory, 1974.

[20] Donna Price. Gap Tests and How They Grow. In *Minutes of the Explosives Safety Seminar (22nd)*, volume 1, pages 365–380, Aneheim, California, August 1986.

[21] Alexander S. Tappan. Microenergetics: Combustion and Detonation at Sub-Millimeter Scales. *AIP Conference Proceedings*, 955:997–1002, 2007.

[22] Alexander S. Tappan, Robert Knepper, Ryan R. Wixom, Jill C. Miller, Michael P. Marquez, and J. Patrick Ball. Critical Thickness Measurements in Vapor-Deposited Pentaerythritol Tetranitrate (PETN) Films. In *14th International Detonation Symposium*, pages 1087–1095, Coeur d'Alene, Idaho, April 2010.

[23] Robert Knepper, Alexander S. Tappan, Ryan R. Wixom, and Mark A. Rodriguez. Controlling the Microstructure of Vapor-Deposited Pentaerythritol Tetranitrate Films. *Journal of Materials Research*, 26(13):1605–1613, 2011.

[24] Donald M. Mattox. *Handbook of Physical Vapor Deposition (PVD) Processing*. Elsevier Inc., 2nd edition, 2010.

[25] Robert Knepper, Michael P. Marquez, and Alexander S. Tappan. Effects of Confinement on Detonation Behavior of Vapor-Deposited Hexanitroazobenzene Films. In *Proceedings of the 15th International Detonation Symposium*, San Francisco, California, July 2014.

[26] Robert Knepper, Ryan R. Wixom, Michael P. Marquez, and Alexander S. Tappan. Near-Failure Detonation Behavior of Vapor-Deposited Hexanitrostilbene (HNS) Films. *AIP Conference Proceedings*, 1793:030014, 2017.

[27] Ryan R. Wixom, Alexander S. Tappan, Gregory T. Long, Anita M. Renlund, Eric J. Welle, Joel P. Mcdonald, Bradley H. Jared, Aaron L. Brundage, and Joseph R. Michael. Microenergetics: Characterization of Sub-Millimeter PETN Films. In *35th International Pyrotechnics Seminar and Symposium,*, pages 181–192, Ft. Collins, Colorado, July 2008.

[28] U. S. Department of Energy. DOE Standard Explosives Safety. Report No. DOE-STD-1212-2012, Washington, DC, June 2012.

[29] Henry Eyring, Richard E. Powell, George H. Duffey, and Ransom B. Parlin. The Stability of Detonation. *Chemical Reviews*, 45(1):69–181, 1948.

[30] A. W. Campbell, W. C. Davis, J. B. Ramsay, and J. R. Travis. Shock Initiation of Solid Explosives. *The Physics of Fluids*, 4:511–521, 1961.

[31] P. Howe, R. Frey, B. Taylor, and V. Boyle. Shock Initiation and the Critical Energy Concept. In *Proceedings of the 6th Symposium (International) on Detonation*, Coronado, California, August 1976.

[32] B. A. Khasainov, B. S. Ermolaev, H. N. Presles, and P. Vidal. On the Effect of Grain Size on Shock Sensitivity of Heterogeneous High Explosives. In *Shock Waves*, volume 7, pages 89–105, 1997.

[33] Alexander S. Tappan, Ryan R. Wixom, and Robert Knepper. Geometry Effects on Detonation in Vapor-Deposited Hexanitroazobenzene (HNAB). *AIP Conference Proceedings*, 1793:030036, 2017.

[34] Alexander S. Tappan, Anita M. Renlund, Gregory T. Long, Stanley H. Kravitz, Kenneth L. Erickson, Wayne M. Trott, and Melvin R. Baer. Microenergetic Processing and Testing to Determine Energetic Material Properties at the Mesoscale. In *12th International Detonation Symposium*, San Diego, California, August 2002.

[35] Omkar A. Nafday, Rajasekar Pitchimani, and Brandon L. Weeks. Patterning High Explosives at the Nanoscale. *Propellants, Explosives, Pyrotechnics*, (5), 2006.

[36] Alexander S. Tappan, Robert Knepper, Ryan R. Wixom, Michael P. Marquez, J. Patrick Ball, and Jill C. Miller. Critical Detonation Thickness in Vapor-Deposited Pentaerythritol Tetranitrate (PETN) Films. *AIP Conference Proceedings*, 1426:677–680, 2012.

[37] Terry R. Gibbs and Alphonse Popolato, editors. *LASL Explosive Property Data*. University of California Press, Ltd., 1980.

[38] John Starkenberg and Toni M. Dorsey. An Assessment of the Performance of the History Variable Reactive Burn Explosive Initiation Model in the CTH Code. Report No. ARL-TR-1667, Army Research Laboratory, 1998.

[39] Eric C. Forrest, Robert Knepper, Michael T. Brumbach, Kim Archuleta, Michael P. Marquez, Hy D. Tran, and Alexander S. Tappan. Influence of Surface Contamination on the Microstructure and Morphology of Vapor-Deposited Pentaerythritol Tetranitrate (PETN) Films. In *APS Topical Conference on the Shock Compression of Condensed Matter*, St. Louis, Missouri, July 2017.

[40] Robert Knepper, Eric C. Forrest, Michael P. Marquez, and Alexander S. Tappan. Effect of Microstructure on the Detonation Behavior of Vapor-Deposited Pentaerythritol Tetranitrate (PETN) Films. *AIP Conference Proceedings*, 1979:150022, 2018.

[41] M. D. Thouless. Combined Buckling and Cracking of Films. *Journal of the American Ceramic Society*, 76(11):2936–2938, 1993.

[42] Eric C. Forrest, Julio C. Peguero, Michael J. Hargather, Robert Knepper, Alexander S. Tappan, Michael P. Marquez, Jonathan G. Vasiliauskas, and Stephen G. Rupper. Effect of Microscale Defects on Shock and Detonation Propogation in Pentaerythritol Tetranitrate (PETN) Films. In *Proceedings of the 16th International Detonation Symposium*, 2018.

[43] Gary S. Settles. *Schlieren and Shadowgraph Techniques*. Springer-Verlag, 2001.

[44] Michael J. Hargather and Gary S. Settles. Optical Measurement and Scaling of Blasts from Gram-Range Explosive Charges. *Shock Waves*, 17:215–223, 2007.

[45] Michael J. Hargather. *Scaling, Characterization, and Application of Gram-Range Explosive Charges To Blast Testing of Materials*. PhD thesis, The Pennsylvania State University, 2008.

[46] F. R. Svingala, M. J. Hargather, and G. S. Settles. Optical Techniques for Measuring the Shock Hugoniot Using Ballistic Projectile and High-Explosive Shock Initiation. *International Journal of Impact Engineering*, pages 76–82, 2012.

[47] Mark Lieber, Michael Murphy, and Matthew Biss. On a Physics-Based Model Equation for Shock-Position Evolution in PMMA. *AIP Conference Proceedings*, 1979:160014, 2018.

[48] M. J. Murphy and C. E. Johnson. Preliminary Investigations of HE Performance. In *Journal of Physics: Conference Series*, 2014.

[49] Matthew Biss, Michael Murphy, and Mark Lieber. Qualification of a Multi-Diagnostic Detonator-Output Characterization Procedure Utilizing PMMA Witness Blocks. *AIP Conference Proceedings*, 1979:160005, 2018.

[50] S. A. Clarke, C. A. Bolme, M. J. Murphy, C. D. Landon, T. A. Mason, R. J. Adrian, A. A. Akinci, M. E. Martinez, and K. A. Thomas. Using Schlieren Visualization to Track Detonator Performance. *AIP Conference Proceedings*, 955:1089–1092, 2007.

[51] Kyle O. Winter and Michael J. Hargather. Three-Dimensional Shock Wave Reconstruction Using Multiple High-Speed Digital Cameras and Background-Oriented Schlieren Imaging. *Experiments in Fluids*, 60:93, 2019.

[52] M. N. Skaggs, M. J. Hargather, and M. A. Cooper. Characterizing Pyrotechnic Igniter Output with High-Speed Schlieren Imaging. *Shock Waves*, 27:15–25, 2017.

[53] Charles E. Anderson Jr. An Overview of the Theory of Hydrocodes. *International Journal of Impact Engineering*, pages 33–59, 1987.

[54] David J. Benson. Computational Methods in Lagrangian and Eulerian Hydrocodes. *Computer Methods in Applied Mechanics and Engineering*, 1992.

[55] Ralph Menikoff. On Beyond the Standard Model for High Explosives Challenges and Obstacles to Surmount. *AIP Conference Proceedings*, 1195:18–25, 2010.

[56] Ralph Menikoff and Christina A. Scovel. Systematic Approach to Verification and Validation: High Explosive Burn Models. Report No. LA-UR-12-20591, Los Alamos National Laboratory, 2012.

[57] John Starkenberg. Modeling Detonation Propagation and Failure Using Explosive Initiation Models in a Conventional Hydrocode. In *12th International Detonation Symposium*, San Diego, California, August 2002.

[58] William Von Holle and Charles Martin. Safe Handling of Insensitive High Explosive Weapon Subassemblies at the Pantex Plant. Report No. DNFSB/TECH-24, Defense Nuclear Facilities Safety Board, 1999.

[59] Brendan M. Welch, James E. Fritz, and Steven L. Perkins. Explosive Systems Development Using Hydrocode Modeling. In *American Institute of Aeronautics and Astronautics 33rd Joint Propulsion Conference and Exhibit*, Seattle, Washington, July 1997.

[60] L. Vitos, A. V. Ruban, H. L. Skriver, and J. Kolair. The Surface Energy of Metals. *Surface Science*, (Denmark), 1998.

[61] W. R. Tyson and W. A. Miller. Surface Free Energies of Solid Materials Estimation From Liquid Surface Tension Measurements. *Surface Science*, 62(1):267–276, 1977.

[62] Justin Peatross and Michael Ware. *Physics of Light and Optics*. 2015.

[63] www.newport.com/n/focusing-and-collimating.

[64] John Canny. A Computational Approach to Edge Detection. *IEEE Transactions on Pattern Analysis and Machine Intelligence*, PAMI-8(6):979–698, November 1986.

[65] Karel Zuiderveld. Contrast Limited Adaptive Histograph Equalization. *Graphic Gems IV*, pages 474–485, 1994.

[66] Steven C. Chapra and Raymond P. Canale. *Numerical Methods for Engineers*. McGraw-Hill Education, 2015.

[67] E. L. Lee, H. C. Hornig, and J. W. Kury. Adiabatic Expansion of High Explosive Detonation Products. Report No. UCRL-50422, Lawrence Livermore National Laboratory, 1968.

[68] Michael E. Berger. Detonation of High Explosives in Lagrangian Hydrodynamic Codes Using the Programmed Burn Technique. Report No. LA-6097-MS, Los Alamos National Laboratory, 1975.

[69] Sesame: The Los Alamos National Laboratory Equation of State Database. Report No. LA-UR-92-3407, Los Alamos National Laboratories, 1992.

[70] J. M. McGlaun and S. L. Thompson. CTH: A Three-Dimensional Shock Wave Physics Code. *International Journal of Impact Engineering*, 10:351–360, 1990.

[71] Rafael C. Gonzalez, Richard E. Woods, and Steven L. Eddins. *Digital Image Processing Using MATLAB*. Gatesmark Publishing, 2nd edition, 2009.

[72] J. B. Ramsay and A. Popolato. Analysis of Shock Wave and Initiation Data for Solid Explosives. In *Proceedings of the Fourth International Symposium on Detonation*, White Oak Maryland, October 1965.

[73] Ken Black. *Buisness Statistics for Contemporary Decision Making*. John Wiley and Sons, Inc., 8th edition, 2013.

[74] William C. Davis. Shock Desensitizing of Solid Explosive. In *Proceedings of the 14th International Detonation Symposium*, Coeur d'Alene , Idaho, April 2010.

Measurement of Shock and Detonation Propagation Along Pentaerythritol Tetranitrate (PETN) Thin Films

by

Julio C. Peguero II